The flow structure in the near field of jets and its effect on cavitation inception

By SHRIDHAR GOPALAN,
JOSEPH KATZ AND OMAR KNIO

Department of Mechanical Engineering,
The Johns Hopkins University, Baltimore, MD 21218, USA

Cavitation experiments performed in the near field of a 50 mm diameter (D) jet at $Re_D = 5 \times 10^5$, showed inception in the form of inclined 'cylindrical' bubbles at axial distances (x/D) less than 0.55, with indices of 2.5. On tripping the boundary layer, cavitation inception occurred at $x/D \approx 2$, as distorted 'spherical' bubbles with inception indices of 1.7. To investigate these substantial differences, the near field of the jet was measured using PIV. Data on the primary flow, the strength distribution of the 'streamwise' vortices and the velocity profiles within the initial boundary layers were obtained. The untripped case showed a direct transition to three-dimensional flow in the near field ($x/D < 0.7$) even before rolling up to distinct vortex rings. Strong 'streamwise' vortices with strengths up to 25% of the jet velocity times the characteristic wavelength were seen. Cavitation inception occurred in the core of these vortices. In contrast, in the tripped jet the vortex sheet rolled up to the familiar Kelvin–Helmholtz vortex rings with weak secondary vortices. Using the measured nuclei distribution, strengths and straining of the 'streamwise' structures, the rates of cavitation events were estimated. The estimated results match very well the measured cavitation rates. Also, the Reynolds stresses in the near field of the jet show similar trends and magnitudes to those of Browand & Latigo (1979) and Bell & Mehta (1990) for a plane shear layer.

1. Introduction and background

This paper deals with the onset of cavitation and the associated near-field flow structure in circular jets at high Reynolds numbers. It is well known that cavitation inception occurs when a nucleus (e.g. microscopic bubble or particle with air trapped in its crevices) is exposed to a sufficiently low pressure to cause unstable growth and collapse of the cavity (Arndt 1981 and Brennen 1995). Rigorous cavitation inception criteria have been recently discussed in Joseph (1998). Thus, the onset of cavitation is dependent on the availability of nuclei and, being dependent on pressure, is affected by the presence of vortical structures in the flow. In the present paper we focus on the flow structure while controlling the nuclei content by careful seeding.

Typically, a turbulent shear layer contains primary (spanwise) and secondary vortices (Konrad 1976; Breidenthal 1981; Jimenez 1983; Bernal 1981; Jimenez, Cogollos & Bernal 1985; Bernal & Roshko 1986; Lasheras, Cho & Maxworthy 1986) and numerous studies (Kermeen & Parkin 1957; Ooi & Acosta 1983; Johnson *et al.* 1982; Katz 1984; Katz & O'Hern 1986; O'Hern 1990; Ran & Katz 1991, 1994; Belahadji, Franc & Michel 1995; Pauchet, Retailleau & Woillez 1992 and others mentioned in a

detailed review by Arndt 1981) have focused on the relationship between these structures and cavitation. In small jets and small separated regions (Ooi & Acosta 1983; Johnson *et al.* 1982; Ran & Katz 1994) cavitation inception occurs in the core of primary vortex structures that develop as the shear layer rolls up. However, as the size and the characteristic Reynolds number of the separated region increase, especially in plane shear flows, cavitation occurs with increasing frequency in the secondary, axial vortices (Katz & O'Hern 1986; O'Hern 1990; Belahadji *et al.* 1995). In these cases, cavitation extends into the primary structures only at ambient pressures that are considerably lower than the inception level.

1.1. *Some observed trends in the onset of cavitation*

The conditions for cavitation inception are typically indicated by the cavitation inception index,

$$\sigma_i \equiv \frac{P_{0i} - P_v}{\rho V_j^2 / 2} \qquad (1)$$

where P_{0i} is the mean static pressure at inception, P_v is the vapour pressure of the liquid, V_j is the jet velocity and ρ is the liquid density. In plane shear layers and massively separated regions, the overall trend is an increase in the cavitation inception index with Reynolds number especially for $Re < 10^6$ (e.g. Kermeen & Parkin 1957; Katz & O'Hern 1986; Arndt 1995). However, the data are quite scattered as the Reynolds number approaches 10^6, and it is not clear whether the growth rate reaches some plateau. For submerged jets, figure 1 shows a curious trend of σ_i with the jet diameter. This plot is a revised version of the data presented in Ran & Katz (1994). In spite of containing data collected by a variety of detection means (many of them visual under stroboscopic light), nozzle and orifice geometries, Reynolds numbers, dissolved air contents and nuclei distributions, the cavitation inception index clearly increases with the jet diameter. Trends with velocity, on the other hand, are conflicting. In some studies the cavitation inception index increases with velocity (Johnson *et al.* 1982); in others it decreases (Kobayashi 1967; Ran & Katz 1994) and in certain studies both trends occur (Pauchet *et al.* 1992) depending on the Reynolds number. Thus, the trend of σ_i with diameter is not simply a Reynolds number effect.

Insufficient understanding of the underlying flow, especially at relevant scales and Reynolds numbers, has made it difficult to explain these trends. It should be noted here that difficulties in prediction of the inception indices and the number of cavitation events occur also in other forms of cavitation. Specifically, studies by Kuhn de Chizelle, Ceccio & Brennen (1995) and Liu & Brennen (1998) focus on attempts to predict inception trends of travelling bubble cavitation. They also observe an increase in σ_i with increasing model size but not with velocity. They attempt to explain this trend, with partial success, by differences in the trajectories and pressure fields to which the nuclei are exposed as they travel along the model. These models account for some of the relative motion between the bubble and the liquid due to, for example, adverse pressure gradients near the stagnation point. However, they do not account for the details of the boundary layer structure, occurrence of transition to turbulence and impact of the bubble on the local flow. Thus, even in cases where the pressure field without cavitation is known, there are still problems with scaling trends of cavitation inception.

Katz & O'Hern (1986) and O'Hern (1990) studied cavitation phenomena in the turbulent shear layer behind a sharp-edged plate at Reynolds numbers up to 2×10^6.
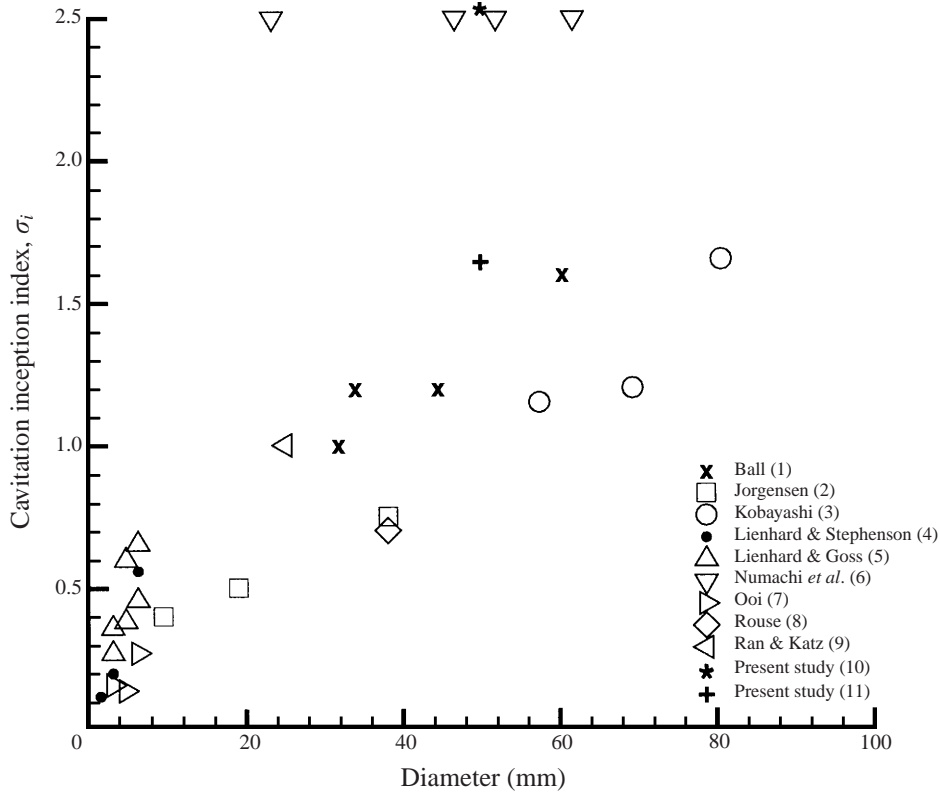
FIGURE 1. Measured cavitation inception indices in jets under different conditions: (1) pipeline orifices based on exit velocity and pressure downstream; (2) nozzles based on exit velocity and pressure downstream; (3) standard nozzles based on exit velocity and pressure downstream; (4) orifices based on the pressure and velocity in the vena contracta; (5) orifices based on average velocity and orifice back pressure; (6) orifices based on pressure downstream and average velocity through orifice; (7), (8), (9) nozzle in a large container; (10) smooth (untripped) nozzle in a large container; (11) tripped nozzle at same conditions as (10). See Ran & Katz (1994) for references.

They found that streamwise vortices control cavitation inception, indicating that the lowest pressure occurs in the core of these vortices. Using microbubbles as pressure sensors (a technique introduced by Ooi & Acosta in 1983), O'Hern (1990) measured normalized negative pressure fluctuations of 250%–300% of the free-stream dynamic pressure. These results explained their measured high cavitation inception indices. Ran & Katz (1994) measured the pressure field (also using microscopic bubbles) and cavitation inception indices in the near field of a 25 mm jet at $Re \sim 4 \times 10^5$. They found that maximum negative pressures occurred in the primary vortices during pairing, where cavitation inception occurred. Their measured normalized pressure fluctuations of -0.99 matched well with the cavitation inception indices.

The present work started as a continuation of this effort by performing tests at a similar Re_D ($= 5 \times 10^5$) but with a 50 mm nozzle, to study the effect of scale on the onset of cavitation. As discussed in Hussain (1986) and Hussain & Zedan (1978), there are two characteristic length scales in the near field of jets, namely the jet diameter D and the momentum thickness of the separating boundary layer Θ. To examine the effect of Θ/D (i.e. to see the effect of changing the characteristics of the

initial boundary layer) on cavitation, experiments were performed with and without boundary layer tripping. It was observed that, for the untripped (or smooth) jet, cavitation inception occurred in the near field ($x/D < 0.6$), in what appeared to be secondary riblets with a cavitation inception index of 2.5. However, in the tripped jet cavitation inception appeared at $x/D \sim 2$ in primary vortices, with inception indices of 1.7.

In order to investigate the causes for such substantial differences on tripping the boundary layer, the focus of this research shifted to the near-field flow structure, with and without boundary layer tripping. Consequently, we used particle image velocimetry (PIV) to measure the primary and secondary flows in the jet shear layer, within $x/D < 1$. The velocity profiles of the separating boundary layer for the smooth and tripped jets also were measured to complete the picture. The data for the smooth jet show that, $x/D < 0.6$ is dominated by strong three-dimensional structures (with a resemblance to hairpin vortices), where cavitation inception occurs. In contrast, in the tripped jet, the separating boundary layer rolls up into classical Kelvin–Helmholtz vortex rings with weak secondary vortices. These results are similar to those of Bell & Mehta (1990, 1993) who performed experiments in plane shear flows with tripped and undisturbed boundary layers. It was shown that plane mixing layers originating from laminar boundary layers were found to contain relatively stronger, organized and large-scale three-dimensionality in the form of streamwise vorticity (these data are at higher axial locations than ours). Their measurements of turbulent stresses in the near field (at axial locations similar to ours) also show trends and magnitudes similar to our data.

The structure of this paper is as follows. Section 2 deals with the experimental apparatus and procedures for particle image velocity measurements. Section 3 explains cavitation inception measurements and results. Phase-averaged distributions of the injected bubbles in the shear layer under non-cavitating conditions are discussed in §4. Section 5 provides the results obtained from PIV measurements of the primary flow. Results obtained from PIV measurements of the secondary flow are discussed in §6. Velocity profiles of the separating boundary layer are discussed in §7. Estimation of peak negative pressure peaks and rate of cavitation events are presented in §8 followed by conclusions in §9.

2. Experimental setup and procedures

The experiments were performed in a specially designed closed-loop jet-cavitation facility located at Johns Hopkins University (figure 2). The main test chamber is 1.98 m long and its cross-section is $0.69 \times 0.76\,\text{m}^2$. It has windows on four sides to enable easy access for PIV and holographic measurements. The flow is driven by two 15 HP centrifugal pumps located about 4 m below the nozzle in order to prevent pump cavitation. An inverter controlled the r.p.m. of one of these pumps, and the flow rate could be regulated. An electromagnetic flowmeter measured the flow rate. The pressure in the test chamber was controlled with a vacuum pump and a source of compressed air. The facility can accommodate jets up to 10 cm in diameter, flow rates up to $391\,\text{s}^{-1}$, and variable pressure in the range 20–400 kPa. The Reynolds number based on jet diameter could reach about 10^6, with operating speeds in the range 10–30 m s^{-1}. In this study the jet velocity was fixed at 10 m s^{-1} ($Re_D = 5 \times 10^5$) and the cavitation index was varied by varying the pressure in the test chamber. The air content was reduced to about 3 p.p.m. by keeping the facility under vacuum for extended periods; the dissolved oxygen content was deter-
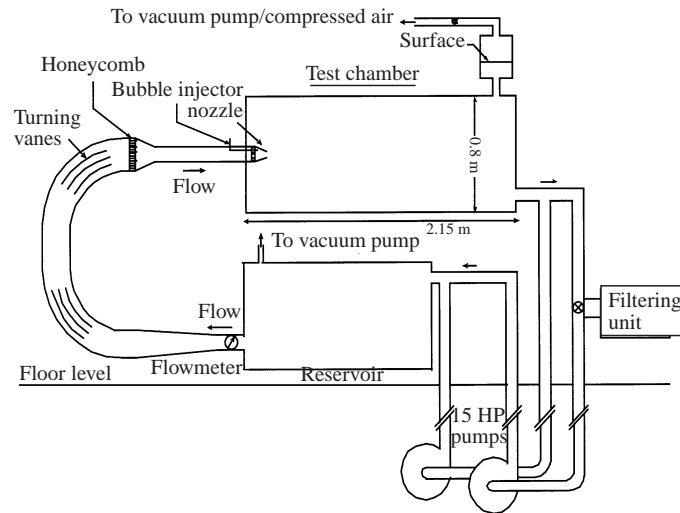
FIGURE 2. Schematic description of the experimental facility.

mined using an oxygen meter. Under these conditions, almost all of the free-stream bubbles larger than 10 μm in diameter were removed. Honeycombs and screens were used for turbulence reduction in the settling chamber upstream of the nozzle. The nuclei for cavitation (air bubbles) were supplied using 5–20 μm diameter capillary glass tubes that were stretched under heat (Ran & Katz 1991). These injectors were typically installed inside the honeycombs, and the bubble injection rate ($\sim 16000\,\mathrm{s}^{-1}$) was controlled by varying the injector nozzle size and gas pressure using a fine metering valve. The injected bubbles were 150–200 μm in diameter and were injected such that they would exit from the potential core and then quickly migrate into the shear layer very close to the nozzle. This procedure is important to ensure that cavitation is not inhibited by lack of nuclei in the shear layer.

A piezo-electric pressure transducer (PCB 102A05) with a resonance frequency of 300 kHz, located close to but outside the jet, sensed the motion of large-scale vortices and was used to record data at specific phases (i.e. conditional sampling of data). Typically, data were recorded either at the positive peak (between two eddies) or the negative peak (an eddy near by) of the pressure signal. The pressure transducer also was used for detecting the occurrence of cavitation. Figure 6 shows sample pressure transducer signals without and with a single cavitation event. The low-frequency part of the signal is caused by the motion of large eddies. For most experiments, the transducer was located at $x/D = 0.375$, $r/D = 0.7$ in both the smooth and tripped cases, so that results at the same phase can be compared (figure 3, which also shows the coordinate system). This location was chosen based on the results obtained from cavitation inception measurements (§ 3).

The 50.8 mm diameter jet was injected from a smooth 2 : 1 diameter ratio cosine-shaped circular nozzle. The length of the nozzle is 76.2 mm. For experiments with a tripped boundary layer an extension tube was attached at the exit of the original nozzle as shown in figure 4. This extension has 16 circumferential axisymmetric trips (i.e. ring-like protrusions) of height 0.5 mm in a 6.35 mm region and the remaining 19 mm wall is smooth.
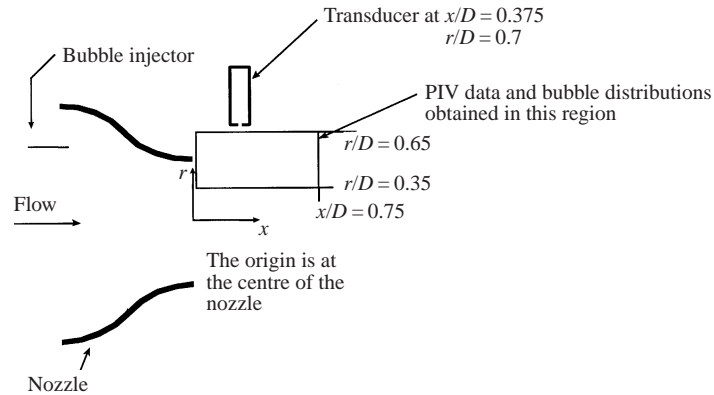
FIGURE 3. Close-up sketch of the region where data were recorded.
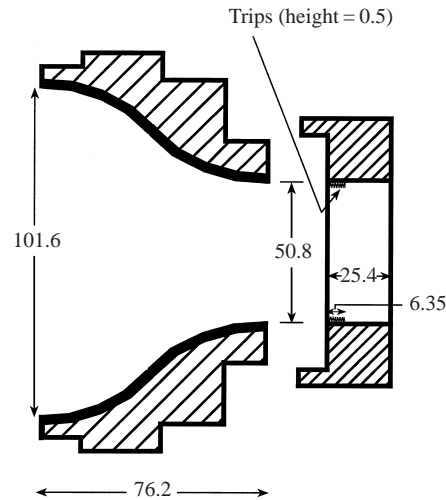
FIGURE 4. Dimensions in mm of the nozzle and extension with trips.

2.1. *Particle image velocimetry* (*PIV*)

Velocity measurements were performed using particle image velocimetry, following procedures detailed in Dong, Chu & Katz (1992), Roth, Hart & Katz (1995) and Sridhar & Katz (1995). Detailed background on PIV can be found in Adrian (1991). This method consists of recording multiple (in this case, double) exposure images of particle tracers in a flow field illuminated by a pulsed laser sheet. The displacement of the particle during the known time interval then gives the local velocity. The laser used was a two-head frequency-doubled Nd : YAG laser (wavelength = 532 nm), capable of pulse energies up to 300 mJ.

2.1.1. *Measurements of the primary flow*

Two-dimensional images of the shear layer at specific phases were recorded on 35 mm film (3200 TMAX) using a still camera. The plane of the light sheet coincided with the centreline of the nozzle (azimuthal angle $\Phi = 90°$ measured from the horizontal) and cut through the spanwise vortex structures in the shear layer (figure 3). The field of view of these images extend from $x/D = 0$ to 1.3 (data were analysed

up to $x/D = 0.7$) and from $r/D = 0$ to 0.85. The tracer particles used were fluorescent of sizes 20–45 µm. These 'in-house' produced particles are neutrally buoyant (specific gravity between 0.95 and 1.05) in water, absorb energy at 532 nm and emit light at 573 nm, i.e. in the yellow range. Hence, if required, one can distinguish between particles and the bubbles, as the latter scatter incident light (Sridhar & Katz 1995). To resolve the directional ambiguity associated with single-frame PIV, initially we used an electro-optic image shifter, which uses a ferroelectric liquid crystal to rotate the polarization and a birefringent crystal to shift the image (Bertuccioli, Gopalan & Katz 1996). In this technique, the second pulse (or image) is shifted with respect to the first by a known positive displacement, which is greater than the highest negative displacement expected in the flow. Once the displacements are computed using the auto-correlation program, the induced displacement is subtracted to get the actual flow field. The fixed image shift induced by the electro-optic image shifter was approximately 1 mm. During the course of this study a 2048×2048 pixel^2 digital camera with hardware-based image shifting became available (Sinha & Katz 1998). The camera records one image and then starts shifting it on the CCD array by the prescribed number of lines after which it stops and waits for the second exposure. The image shift could be performed in steps of 4 lines ranging from 1 to 509 lines and requires 7.2 µs per line to shift.

2.1.2. *Conditional sampling and data analysis*

The signal of the pressure transducer was used to obtain data at specific phases. The two phases chosen were either the positive peak (between two eddies) or the negative peak (an eddy nearby) of the pressure signal. However, most of the data were sampled at a positive pressure peak since cavitation inception in the smooth jet occurred in the vicinity of the transducer (at $x/D = 0.375$), primarily during a positive pressure peak. In order to acquire data at specific peaks of the pressure signal, a custom-built electronic device, which in principle is a differentiator circuit, was used. The signal from the pressure transducer was fed to this device through a low-pass filter (cut-off at 1 kHz) to reduce high-frequency effects. The phase lag due to the low-pass filter and other components in the circuit was resolved by providing (i) adjustable gain for the differentiated output and (ii) adjustable reference for the comparator. By fine tuning (i) and (ii), we found the success rate of this device in obtaining data during peaks to be about 70%–80% (a photodiode was used to check the locations of the light pulses with respect to the pressure signal, during the experiment). Only the data recorded during peaks were used.

For the data recorded using a film camera, the negatives were digitized at a resolution of 3072×2048 pixels using a Nikon LS3500 slide scanner. An auto-correlation technique was used to determine the displacements from the double-exposed images. Calibration experiments (Dong *et al.* 1992; Roth *et al.* 1995) have shown that the uncertainty level can be kept at about 1%, provided certain conditions associated with particle density and magnification are satisfied. Since maximum displacements along the X-axis (after the image shift) were about 2 mm, the interrogation window size that gave the best results was 3.6 mm $\times$ 1.45 mm with a spacing between vectors of 0.72 mm. Within the shear layer there are places with high velocity gradients that are 'trouble spots' for typical PIV analysis. A histogram of the magnitudes of fluctuations in velocity at every node (compared with four of its neighbours) was used to identify the potential trouble spots in the data. In these regions the data were recalculated by individual particle tracking (Sridhar & Katz 1995); if data were not available in the image or was not possible to identify particle pairs, we used an average value
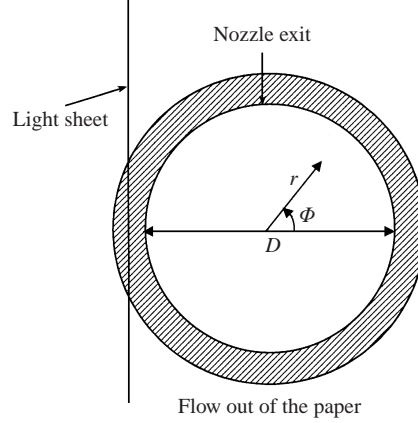
FIGURE 5. Orientation of the light sheet for capturing the 'streamwise' vortices
(i.e. the secondary flow).

from the four neighbours. One could also use multiple correlation peaks in the same
window to identify possible displacements, an idea recently adopted in our 'in house'
PIV code. Vorticity (ω) and strain rates (S_{lm}) were estimated by centre-order finite
differences using

$$\omega(i,j) = \frac{1}{2} \left\{ \frac{u_m(i+1,j) - u_m(i-1,j)}{\Delta x_l} - \frac{u_l(i,j+1) - u_l(i,j-1)}{\Delta x_m} \right\}, \qquad (2)$$

$$S_{lm}(i,j) = \frac{1}{4} \left\{ \frac{u_m(i+1,j) - u_m(i-1,j)}{\Delta x_l} + \frac{u_l(i,j+1) - u_l(i,j-1)}{\Delta x_m} \right\}, \qquad (3)$$

where u_m and Δx_m are the velocity component and grid size in the m-direction. Phase-
averaged velocity, vorticity, shear strain rate, normal stresses $\overline{u'^2}$, $\overline{v'^2}$ and shear stresses
$-\overline{u'v'}$ were obtained from 50 and 57 instantaneous maps for the smooth and tripped
cases respectively. The results are discussed in §5.

2.1.3. *Measurements of the separating boundary layer*

To measure the velocity profile of the separating boundary layer at the exit of the
nozzle ($x/D \sim 0.007$), high-magnification images (magnifications up to 4.5) using a
microscope objective and extension tube, were acquired with the $2K \times 2K$ digital
camera (§2.1.1). The images were shot with a positive pressure peak at $x/D = 0.375$
(although not very relevant here). The entire field of view in this case was 6.3 mm
and an interrogation window covered 200 μm (64 pixels) $\times$ 200 μm with no overlap
between windows. Due to the small field of view, to obtain reasonable accuracy the
particle concentration had to be increased more than for regular PIV. Using 25–40 μm
fluorescent particles caused significant increase in water turbidity (note that there
is a 30 cm of water depth between the laser sheet and the camera). Consequently
we replaced the fluorescent particles with silver-coated glass spheres of size 5–12 μm
(specific gravity 0.9–1.3). Even with the 5–12 μm particles turbidity limited ideal
concentration levels, thus there were some windows with no particles and a typical
window contained 1–2 particles. Within the shear layer the other serious challenge was
that, due to the high magnification, the displacements varied between 13 to 363 pixels
(an image shift of 13 lines was used). Such high displacements and gradients were

resolved by providing the PIV code with an input file containing suitable guess displacements at different coordinates of the image. The results are discussed in §7.

2.1.4. *Secondary flow measurements*

Measurements also were performed with the light sheet in planes parallel to the jet axis, at two positions $r \cos \Phi = 0.53D$ and $0.55D$ as shown in figure 5. These planes cut through the inclined 'streamwise' structures in the shear layer. The vorticity obtained in this plane provides a good estimate of the strengths of these vortices, if the light sheet cuts through the entire vortex. The $2K \times 2K$ digital camera was used to record the images and silver-coated glass spheres were the tracer particles (the 20–45 µm fluorescent particles also could have been used). The field of view of these images was 23 mm; the interrogation window size 900 µm, resulting in 4–5 particle pairs per interrogation window and the spacing between vectors was 539 µm. The results are discussed in §6.

3. Cavitation inception index (σ_i) measurements

The cavitation experiments with the 50 mm jet included measurements of conditions for cavitation inception and observations on the physical appearance of the cavitation. In order to perform controlled experiments, the water in the test chamber was de-aerated to about 3 p.p.m. and filtered through 1 µm filters. Deaeration was performed by lowering the pressure in the facility with the vacuum pump and running the centrifugal pumps at high speed. The air and vapour bubbles generated by pump and jet cavitation were continuously removed from the top of the test chamber by the vacuum pump. After the appropriate dissolved air content was reached, the facility was kept at above atmospheric pressure (with no air–water interface in the test chamber) for one hour before acquiring data. The velocity was fixed at $10 \, \text{m s}^{-1}$ and the ambient pressure in the test chamber was gradually lowered while injecting a uniform train of 150–200 µm bubbles into the shear layer. Two methods were used to detect cavitation events: (*a*) the (trigger or) pressure transducer, (*b*) a video camera equipped with a microscopic objective (and stroboscopic lighting). The field of view of the video images was 10 mm × 12.5 mm. The site of cavitation inception for the smooth and the tripped cases was first identified from these video images recorded at several axial (from $x/D = 0$ to 4.0) (and radial) locations and at different cavitation indices. These sites were found to be $x/D < 0.6$ for the smooth jet and $x/D \approx 2.0$ for the tripped jet. The physical appearances of cavitation and noise spectra are discussed in the next subsection.

Data were acquired such that signals from the pressure transducer and timing of the stroboscope (strobe out) were simultaneously recorded by a data acquisition system (Data Translation A-D converter using GLOBLAB software). An electronic control circuit triggered the stroboscope at 60 Hz (using the video camera signal, for exact synchronization) and fired the stroboscope 200 ms after the data acquisition system was triggered. It also provided one 'reference' blank image every second. This proved useful to correctly match the video images (discrete 60 fields s^{-1}) with the pressure signal that was sampled at 125 kHz. Sections of the transducer signal (see figure 6) were analysed whenever a cavitation event was observed in the video images. This process helped in establishing confidence that, at least at inception levels (less than ~ 10 events s^{-1}), the transducer signal contained traces of every event that was observed visually. There were many events that were missed by the video system but were recorded by the transducer. Subsequently, the transducer signal (located at
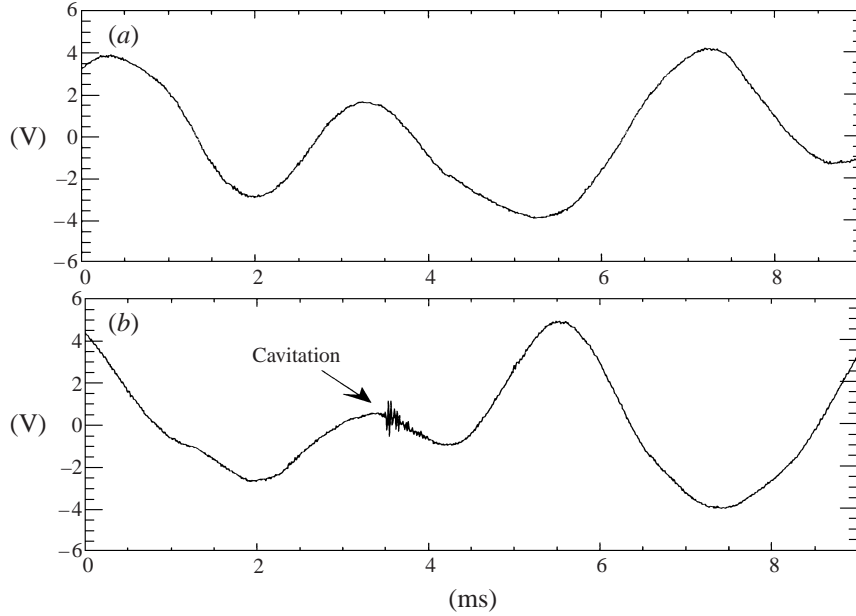
FIGURE 6. Sample pressure signals from the trigger transducer: (*a*) without cavitation (*b*) with one cavitation event.

$x/D = 0.375$ for the smooth jet and $x/D = 1.9$ for the tripped jet) was used to count the number of cavitation events at different cavitation indices (figure 9, which will be discussed shortly).

3.1. *Physical appearance of cavitation and noise spectra*

The video images revealed two forms of cavitation, as shown in figure 7. The first form (figure 7*a*, *b*), that has a shape of inclined 'cylindrical' bubbles, appeared only in the very near field ($x/D < 0.55$) of the smooth (untripped) jet. It did not appear in the tripped jet. A similar type of cavitation had been observed in secondary riblets in the braids of primary vortices in plane shear flows (Katz & O'Hern 1986; O'Hern 1990; Belahadji *et al.* 1995). Consequently, until we performed the velocity measurements, we believed that the events shown in figure 7(*a*, *b*) were also cavitation in the braids. As will be shown shortly, the flow structure in the near field of the smooth jet it considerably more complex. The second form (figure 7*c*) has a shape of distorted, but still fairly 'spherical', large ($\geqslant 0.5\,\mathrm{mm}$) bubbles. This type of cavitation appeared in the core of the primary eddies, both in previous experiments with a 25 mm jet (Ran & Katz 1994) and in the present smooth and tripped 50 mm jets. In the smooth jet it appeared at a considerably lower cavitation index (a discussion follows) compared to the cylindrical bubble cavitation. In the tripped jet it was the only observed form of cavitation inception and appeared at $x/D \sim 2$.

As is already established, during the onset of cavitation the noise spectra have peaks that correspond to the natural frequencies of the bubbles involved. This subject has been discussed in Strasberg (1955) and reviewed in Plesset & Prosperetti (1977) and Brennen (1995). The natural frequency of a spherical bubble is

$$\omega_0 = \left(\frac{3\gamma P_\infty}{\rho R_0^2} + \frac{2(3\gamma - 1)s}{\rho R_0^3} \right)^{1/2} \tag{4}$$
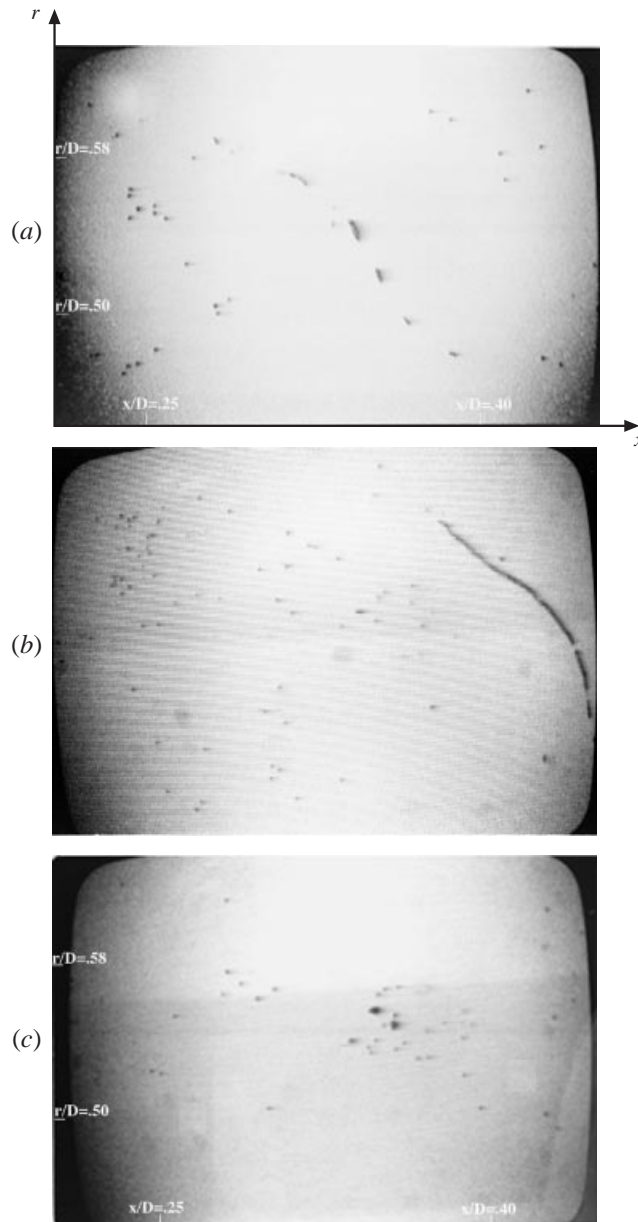
FIGURE 7. (*a*) Cylindrical bubble cavitation observed in the smooth jet during inception stages. (*b*) Cylindrical bubble cavitation observed in the smooth jet when $\sigma = 1.8$. (*c*) Distorted spherical bubble cavitation observed in smooth and tripped cases. Flow is from left to right and the small black dots are the bubbles injected. Note the field of view.

where γ is the polytropic coefficient, s is the surface tension of the liquid, R_0 is the radius of the bubble. Characteristic spectra of the cavitation noise (based on the pressure transducer signal, e.g. figure 6*b*) for the two forms of cavitation (i.e. the 'cylindrical' bubble and the distorted 'spherical' bubble) are presented in figure 8. The distorted spherical bubble has a single peak at 29 kHz, whereas spectra of the cylindrical bubble cavitation have several peaks at 29, 38 and 54 kHz. The 29 kHz
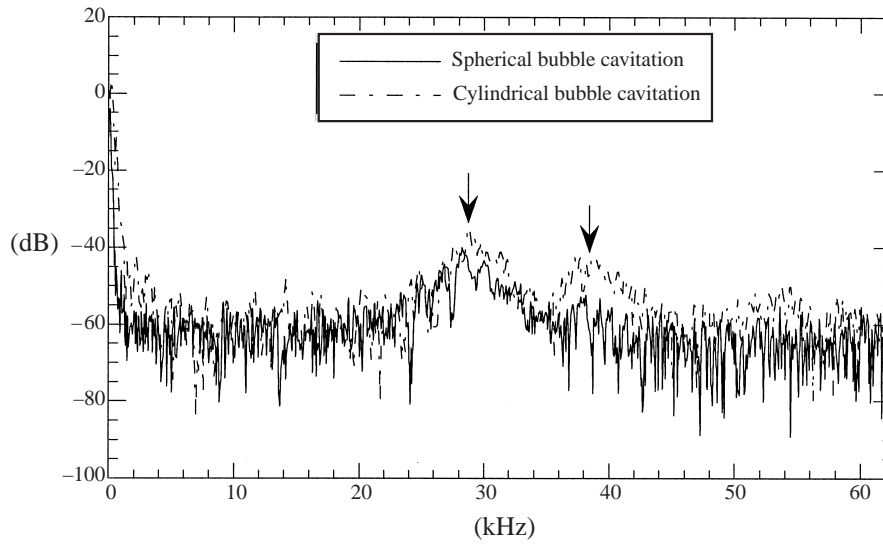
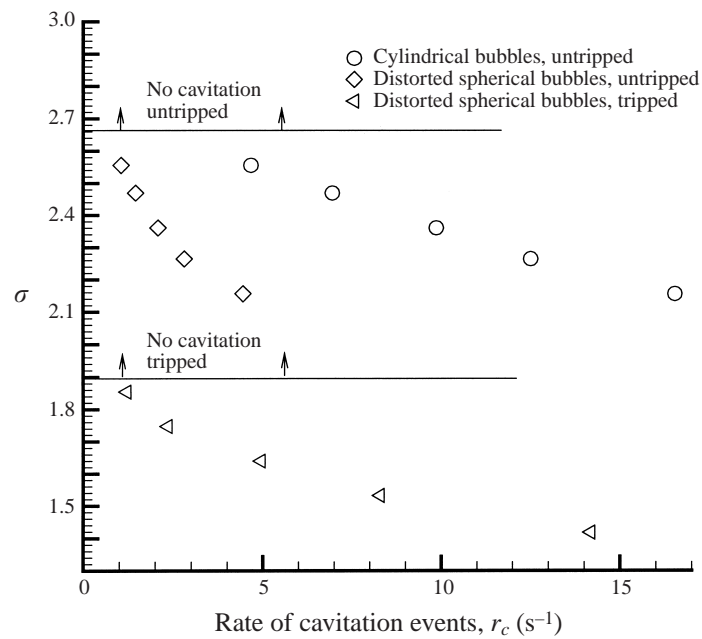FIGURE 8. Spectra of noise for the two forms of cavitation observed in the smooth jet.

FIGURE 9. Measured rate of cavitation events for the smooth and tripped jets.

peak corresponds to the natural frequency of a $200\,\mu m$ bubble (from equation (4)). The trend of multiple spectral peaks, particularly at 29 and 38 kHz when cylindrical bubble cavitation occurred, was consistent in examples for which both video and pressure signals were available. Eventually the spectra were used as a method to differentiate between the two forms of cavitation in the pressure signal. Also note that the spectra of cavitation noise for the tripped jet showed only one peak. By
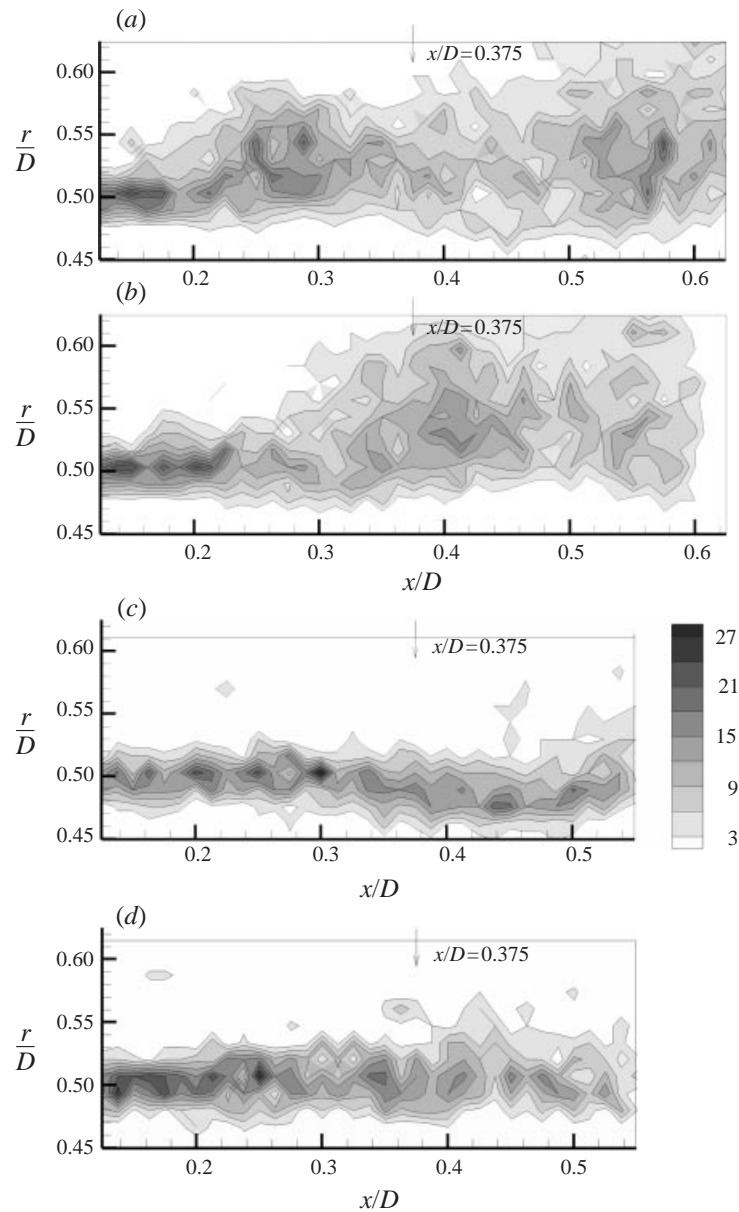
(a)

(b)

(c)

(d)

FIGURE 10. Phase-averaged spatial distributions of bubbles in the near field of the jet. Smooth jet: data recorded at (a) positive pressure peaks, (b) negative pressure peaks. Tripped jet: data recorded at (c) positive pressure peaks, (d) negative pressure peaks. Numbers indicate bubble population in $0.46\,\text{mm}^2$.

examining numerous pressure signals, it was possible to use the spectra to measure the rates of cavitation events. The results, as a function of σ, are plotted in figure 9. It displays the expected increase in the number of events with decreasing σ. For the same rate of events, cavitation indices for the cylindrical bubble cavitation (smooth jet) are significantly higher than those of the spherical bubble cavitation. Finally, the cavitation inception indices of the tripped jet are substantially lower than the results
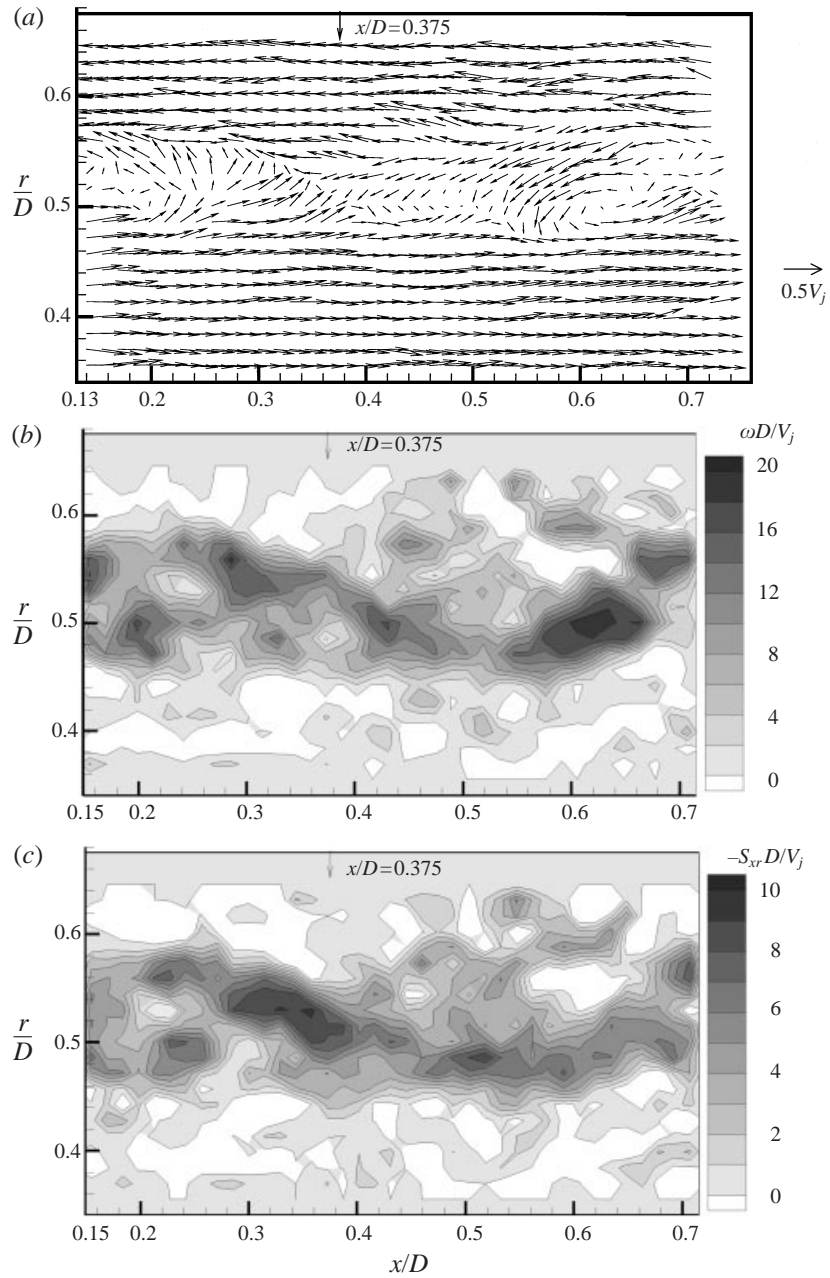
FIGURE 11 (*a–c*). For caption see facing page.

of the smooth jet. It is worth mentioning that all of the results in figure 9, including the tripped jet, are significantly higher than the inception indices for a 25 mm jet ($\sigma_i \sim 1.0$) with a smooth nozzle and at the same Reynolds number (measured by Ran & Katz and shown in figure 1).

These results show an intriguing impact of boundary layer tripping in otherwise the same flow conditions. Since the nuclei supply is very similar, these results indicate major differences in the near-field flow characteristics. The cylindrical bubble cavitation
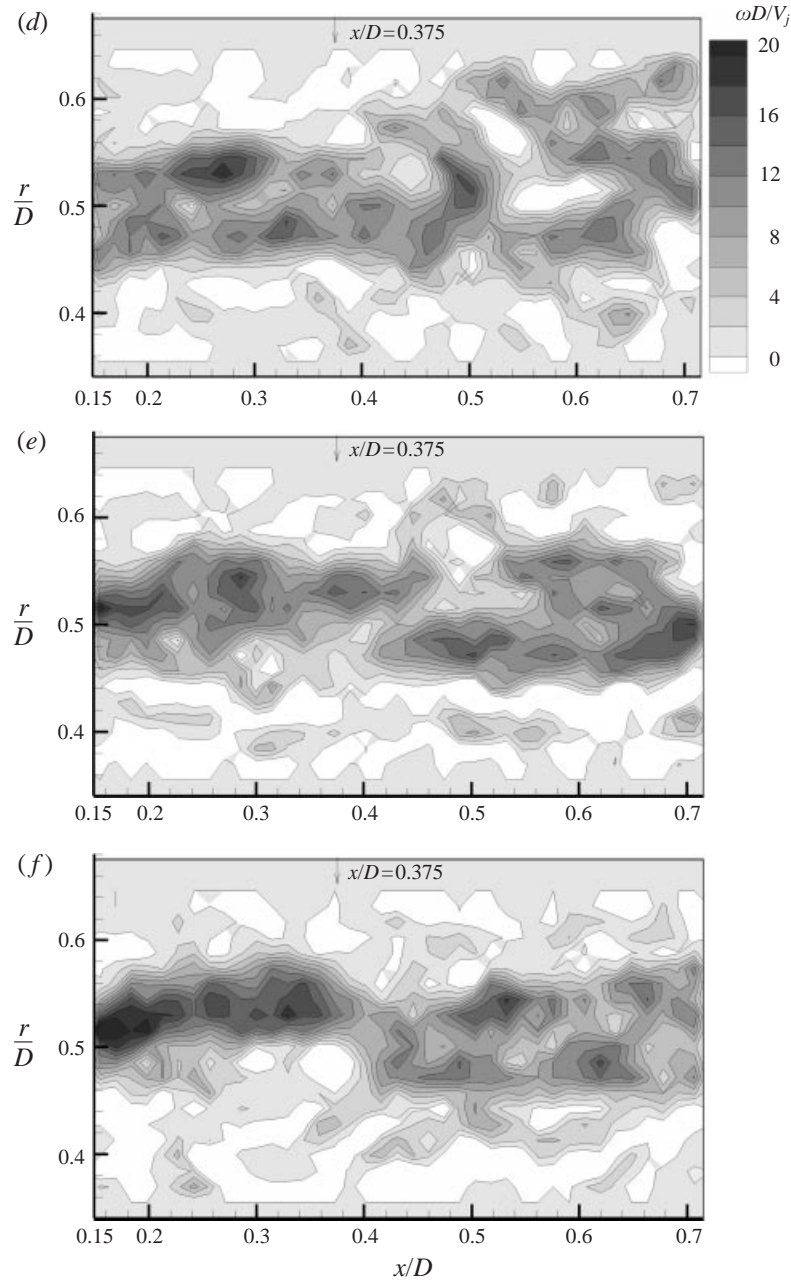
(*d*)

(*e*)

(*f*)

x/D

FIGURE 11. Sample instantaneous (*a*) $\bar{u} - 0.5V_j$, (*b*) normalized vorticity, (*c*) normalized strain, in the smooth jet for data recorded at a positive pressure peak at $x/D = 0.375$. (*d*–*f*) Sample instantaneous normalized vorticity distributions in the near field of the smooth jet to highlight important features. All the plots show a slice through a three-dimensional vortex located at approximately $x/D = 0.3$.

observed in the smooth jet suggests that 'secondary structures' play a more important role in the smooth jet than in the tripped jet. To understand these differences, the near field of the jet ($x/D < 1$) became the primary focus of our research. The transducer was placed at $x/D = 0.375$ in both the smooth and tripped jets to be used as a

trigger for bubble distributions and PIV measurements. Results are discussed in the following sections.

4. Spatial distributions of the injected bubbles under non-cavitating conditions

Since the pressure signal and the stroboscope timing signal could be acquired simultaneously (§ 3), phase-averaged bubble distributions were measured from the silhouette video images under non-cavitating conditions. The images were analysed using a blob-analysis software package (Matrox Inspector) and the locations (centroid) of the bubbles were obtained. Each image contained 20–50 bubbles and by combining sufficient images, all recorded at the same phase, the phase-averaged bubble distributions in the near field of the jet shown in figure 10 were obtained. Though not obvious at the beginning, the phase-averaged bubble distributions do give information about the flow field. They also highlight differences between the smooth and the tripped cases. Some of the observations are as follows. In all the plots, the bubble distributions are non-uniform. The distributions for the positive pressure peak (figures 10a and 10c) show fewer bubbles in the vicinity of $x/D = 0.375$, with higher concentrations on either side. The distributions for the negative pressure peak (figures 10b and 10d) indicate higher bubble populations around the $x/D = 0.375$ region. This shows that the bubbles tend to migrate towards the larger structures in the flow. The bubble clusters in the smooth jet (figure 10a) also indicate a characteristic wavelength of $\lambda = 0.25D$–$0.3D$, whereas the wavelength in the tripped jet (figure 10c) is $\lambda = 0.15D$–$0.2D$. In the smooth jet (figure 10a), the bubbles are scattered over a wider region and high bubble concentrations (or even peaks) extend up to $r/D = 0.55$ at approximately $x/D = 0.3$. Conversely, in the tripped case the bubbles are confined to a narrower region with peaks aligned along $r/D = 0.5$. These plots suggest that the shear layer of the smooth jet extends quite abruptly in the radial direction, whereas in the tripped jet it grows gradually.

5. Near-field flow structure under non-cavitating conditions (PIV data)

Data presented here are the results of the measurement procedures described in § 2.1.1. Figures 11 and 12 show sample instantaneous velocity ($\bar{u} - 0.5V_j$), vorticity perpendicular to the plane of the light sheet (ω), and strain ($-S_{xr}$) for the smooth and the tripped cases respectively when the phase is a positive peak of the pressure signal. An additional three instantaneous vorticity distributions for the smooth jet are presented in figures 11(d)–11(f) to highlight important features of the near field. Fifty and fifty-seven instantaneous velocity maps (all at the same phase) were analysed for the smooth and tripped cases respectively. Corresponding phase-averaged results obtained from these distributions are shown in figures 15 and 16. Sample instantaneous maps for the negative pressure peak are shown in figures 13 and 14. Phase-averaged results for the negative pressure peak phase are not shown.

5.1. *Untripped jet*

The sample velocity map of the smooth jet (figure 11a) shows a saddle point and the vorticity maps (figures 11b, 11d–f) show thinning vorticity, which agree well with a positive pressure peak at $x/D = 0.375$. The vorticity maps also show vorticity peaks which extend to high radial locations, up to $r/D = 0.55$, at approximately $x/D = 0.3$. Note the similarity between this and the phase-averaged
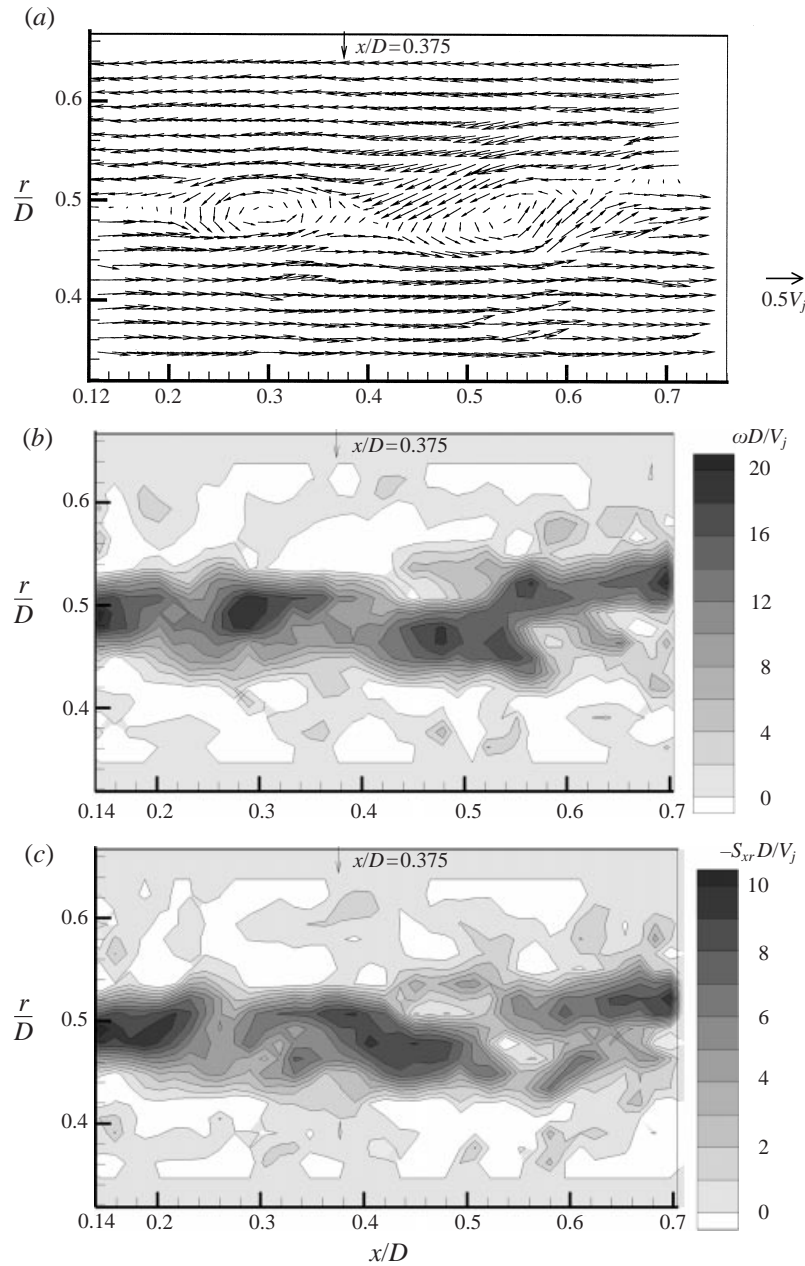
FIGURE 12. As figure 11(*a–c*) but for the tripped jet.

bubble distributions (in figure 10*a*), where high bubble concentrations extended up to $r/D = 0.55$ at a similar axial location. Some of the vorticity maps (figure 11*b*) also show irrotational fluid engulfed between layers of vortical fluid. As will be demonstrated using other interrogation planes (§6), the existence of vorticity peaks at $r/D \geqslant 0.53$, $x/D < 0.5$ is associated with the flow becoming three-dimensional immediately after exiting from the nozzle, even before rolling up to distinct vortex rings. Prominent vortex rings are observed beyond $x/D = 0.75$. At $x/D < 0.5$,
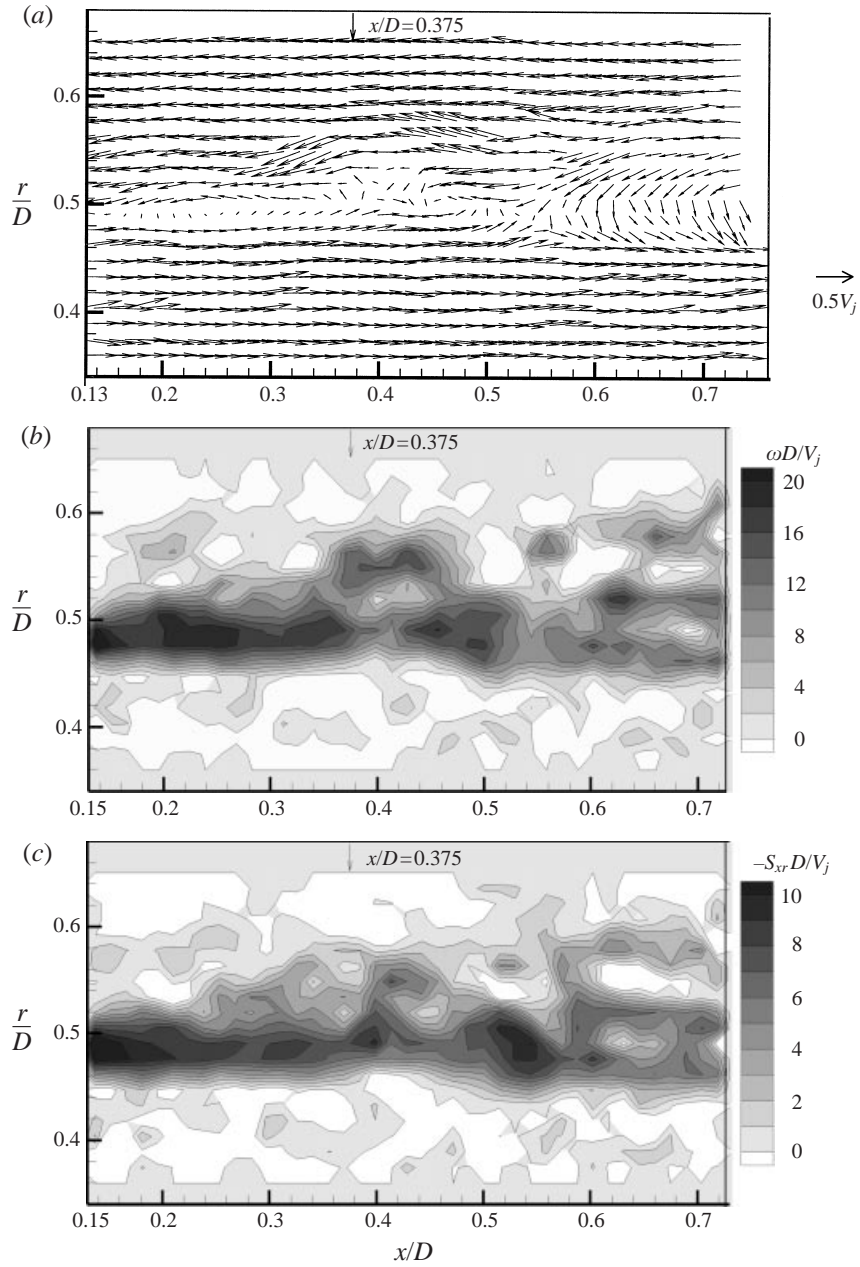
FIGURE 13. Sample instantaneous (*a*) $\bar{u} - 0.5V_j$, (*b*) normalized vorticity, (*c*) normalized strain in the smooth jet for data recorded at a negative pressure peak at $x/D = 0.375$.

the thin, laminar boundary layer separating from the nozzle is highly unstable and portions of this vortex sheet are locally displaced into the external slow moving fluid. These 'bumps' are rapidly stretched by the steep velocity gradient, resulting in the formation of strong 'streamwise' vortices along the principal strain axis. In some cases these structures resemble hairpin vortices, which was noted from counter-rotating vorticity pairs in measurements to be described in §6. Vorticity maps in
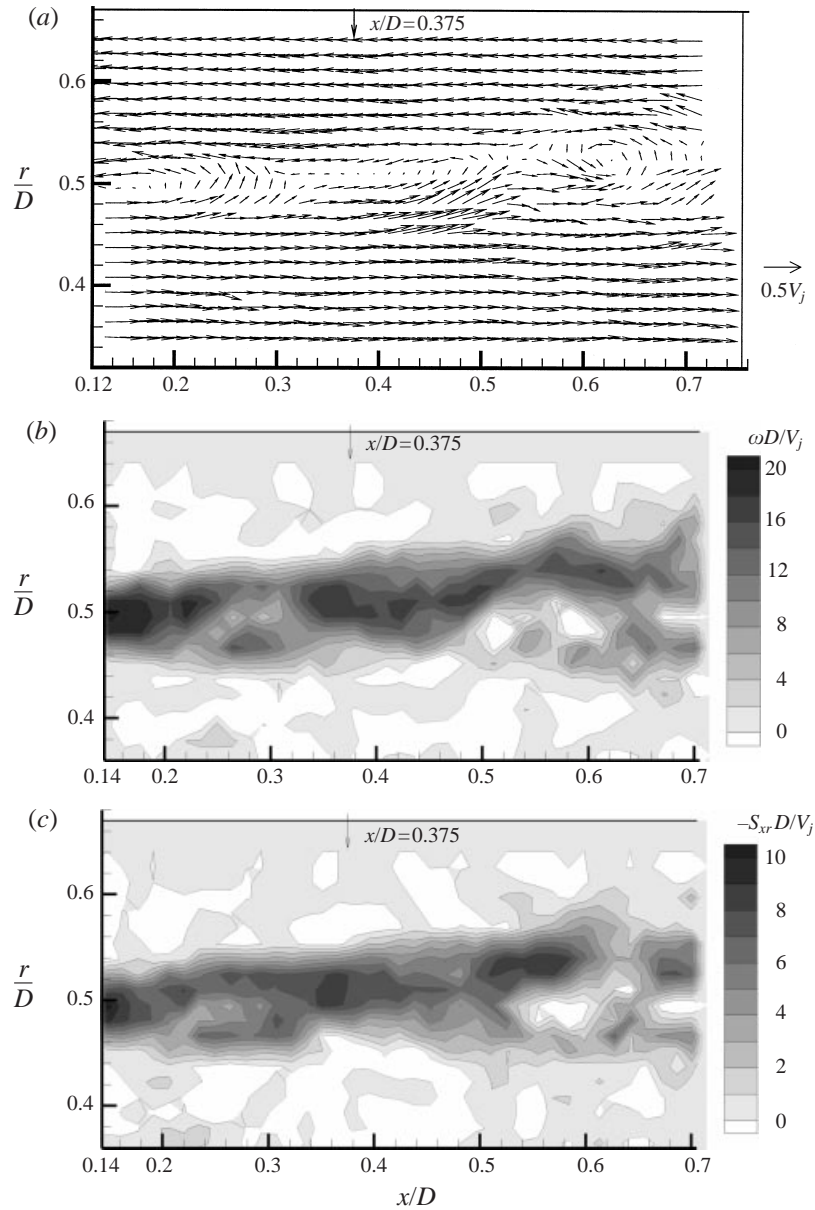
FIGURE 14. As figure 13 but for the tripped jet.

figures 11(b), 11(d–f), show a slice through this three-dimensional vortical structure at approximately $x/D = 0.3$. This near-field behaviour of the smooth jet is very different from roll up to vortex rings typically seen in shear layers, including the present tripped jet. Confirming the results of the bubble distributions, there is also a characteristic wavelength $\lambda = 0.25D$–$0.3D$, that is sensed by the trigger transducer. The strain ($-S_{xr}$) map (figure 11c) shows peak magnitudes in the vicinity of $x/D = 0.375$, but the region of high strain is clearly displaced towards the 'vortex' at $x/D \sim 0.3$.
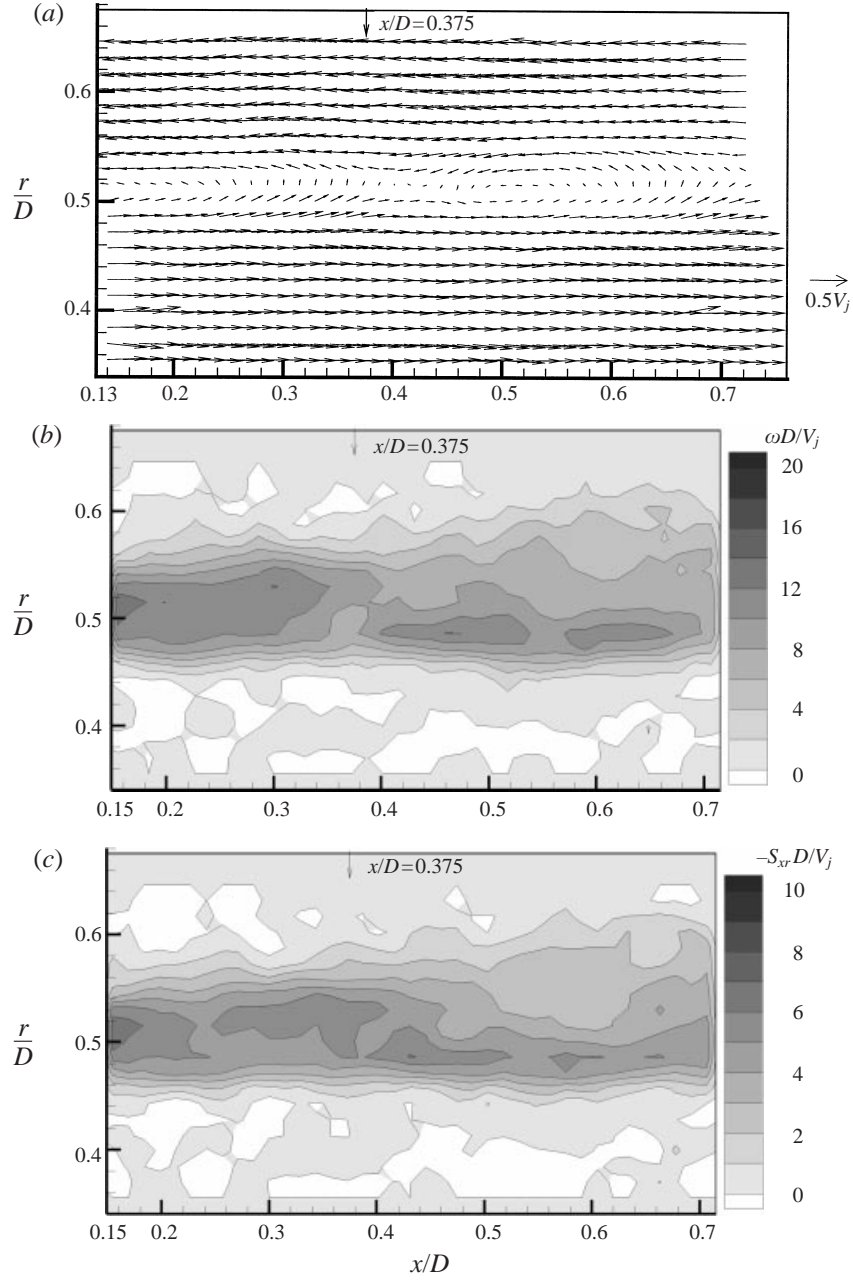
FIGURE 15. Phase-averaged (*a*) $\bar{u} - 0.5V_j$, (*b*) normalized vorticity, (*c*) normalized strain in the smooth jet for data recorded at a positive pressure peak at $x/D = 0.375$.

5.2. *Tripped jet*

The sample velocity map (figure 12*a*), recorded during a positive pressure peak of the trigger transducer, shows a much more orderly structure compared to the smooth case and a saddle point close to $x/D = 0.375$. The vorticity distribution in figure 12(*b*) shows prominent spanwise structures (rings) with peaks roughly aligned along
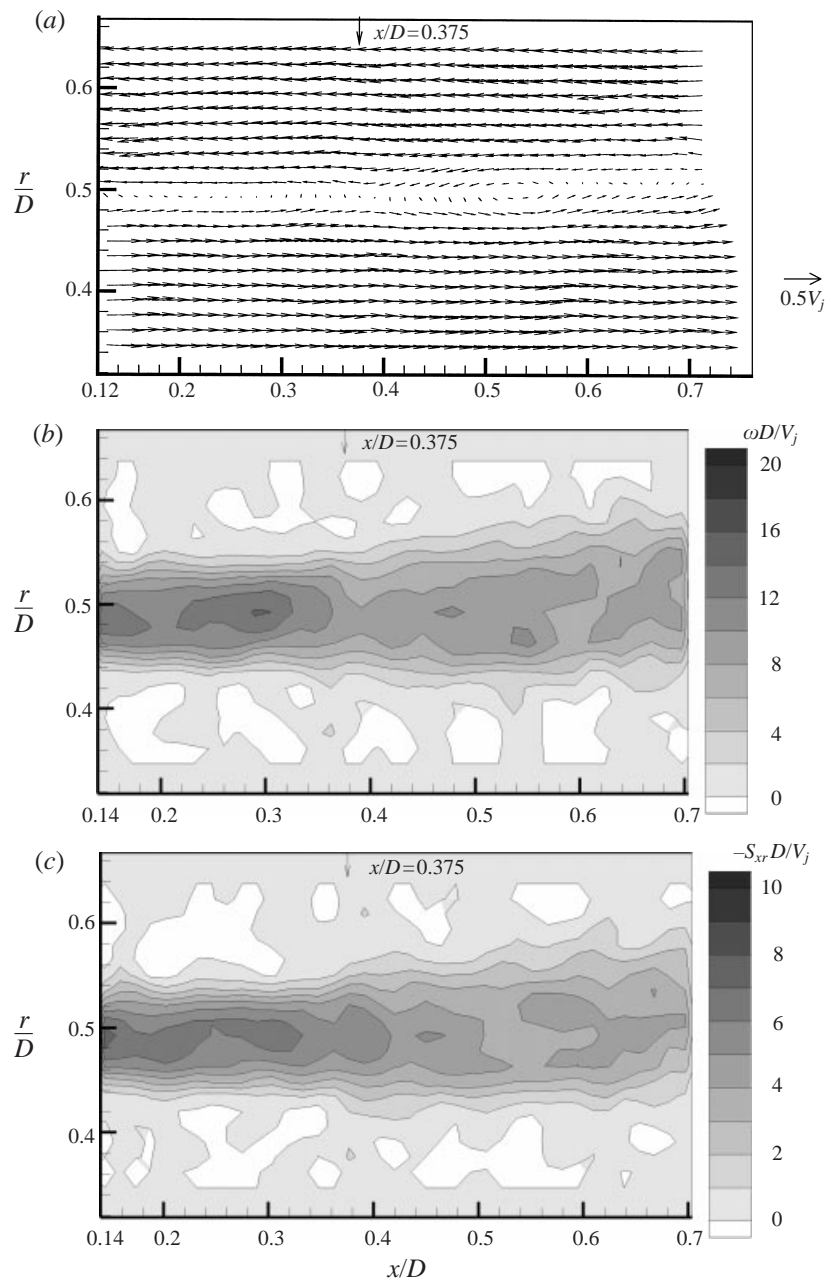
FIGURE 16. As figure 15 but for the tripped jet.

$r/D = 0.5$, quite consistent with a typical shear layer. The thinning vorticity region between the vortex rings coincides well with the location of the trigger transducer. In this sample map, one also can seen vortex pairing at about $x/D = 0.6$. The strain map (figure 12c) shows peak magnitudes in the braid region, well centred between the ring structures. Similar trends in vorticity and strain were seen in the 57 instantaneous maps that were analysed. Thus, in the near field of the tripped jet, the thicker turbulent boundary layer rolls up into prominent Kelvin–Helmholtz vortex rings. Note that the
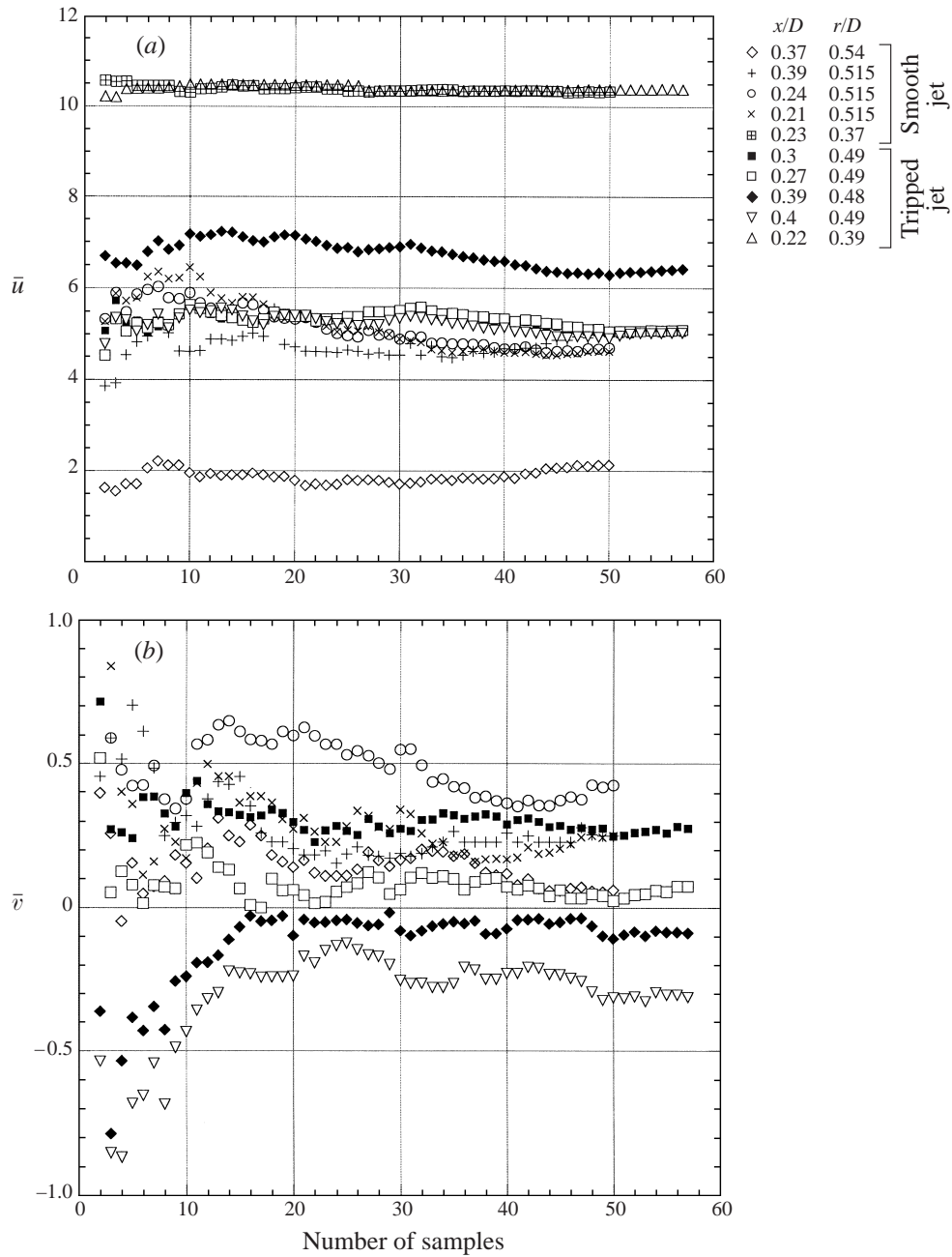
FIGURE 17. Running averages of velocity components (m s^{-1}) for the smooth and tripped jets at random sample points to show convergence of data.

strength of the strain field in the tripped jet is similar to that of the smooth jet (the strain distributions for the two cases are presented in figures 21 and 22 and table 1). Thus, the magnitude of the strain rate (stretching 'secondary' vortices) clearly was not the primary cause for the differences observed in the conditions and appearance for cavitation inception. This indicates that the strengths of the secondary vortices
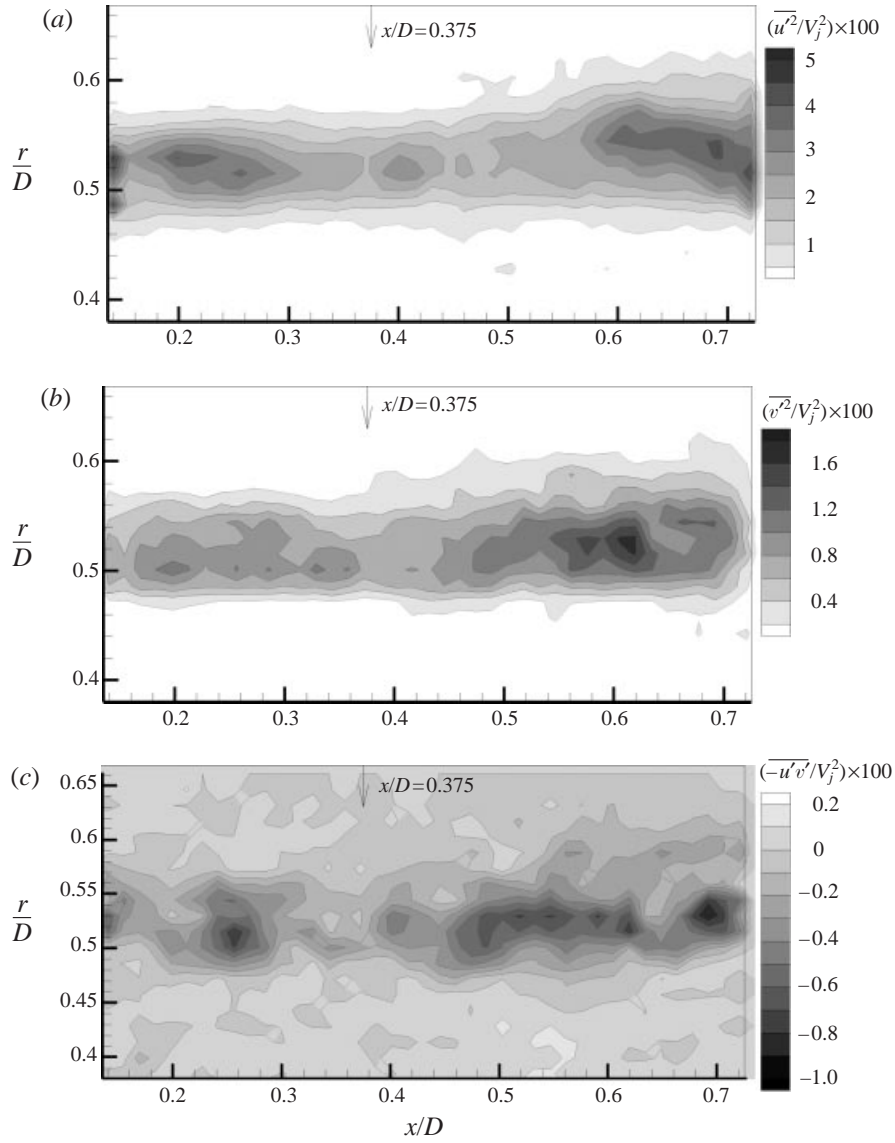
FIGURE 18. Distributions of (*a*) $\overline{u'^2}$, (*b*) $\overline{v'^2}$, (*c*) $-\overline{u'v'}$, in the smooth jet for data recorded at a positive pressure peak at $x/D = 0.375$.

where cavitation inception occurs (figure 7*a*, *b*) must be much higher in the smooth jet than in the tripped case (if they exist at all). This also is evident from the discussion presented in the previous section. This conclusion led to velocity measurements in planes that provide data directly on the strength of these vortices (§6). However, for example, the vorticity peaks (figures 11*b*, 11*d–f*) at $x/D = 0.3$, $r/D = 0.55$ are an indication of this strength, since it cuts through the three-dimensional structure.

The vorticity maps for data recorded during a negative pressure peak (figures 13 and 14) show peak vorticity below the transducer, confirming that the conditional sampling method was successful. Note that in the smooth case the vortical structure is

(a)

$x/D = 0.375$

$(\overline{u'^2}/V_j^2) \times 100$

$\frac{r}{D}$

(b)

$x/D = 0.375$

$(\overline{v'^2}/V_j^2) \times 100$

$\frac{r}{D}$

(c)

$x/D = 0.375$

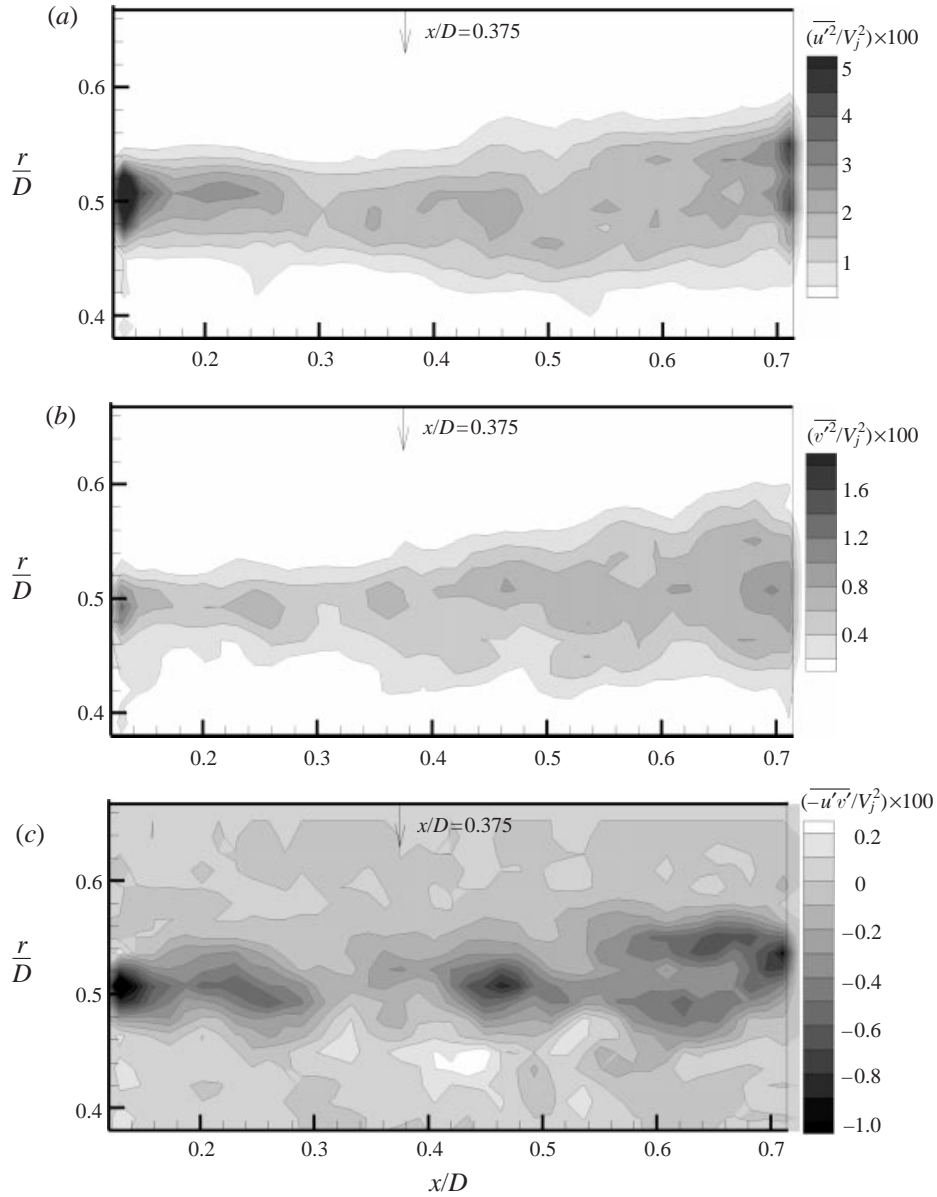$(-\overline{u'v'}/V_j^2) \times 100$

$\frac{r}{D}$

x/D

FIGURE 19. As figure 18 but for the tripped jet.

simply convected to $x/D = 0.375$. The same applies to the tripped jet, but in this case the ring is convected. Besides being convected, these data (or phase) do not provide additional insight and as a result the negative pressure peak data are not pursued further.

Phase-averaged velocity, vorticity and strain for the smooth and tripped jets are displayed in figures 15 and 16 respectively. Running averages of velocity components for points selected inside and outside the shear layer are presented in figure 17. This graph shows the convergence of the phase-averaged velocities as the number of samples is increased. Clearly, convergence is achieved in most cases. Phase averaging
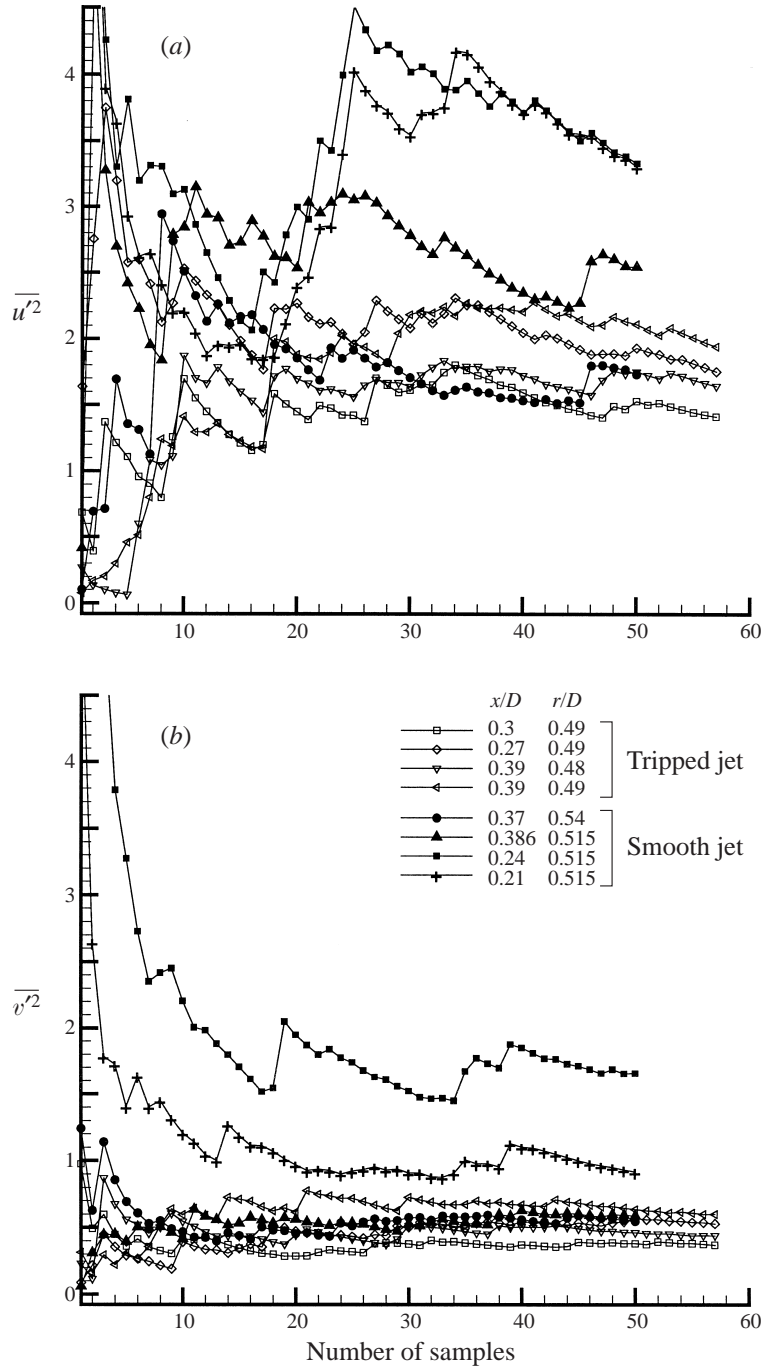
FIGURE 20. Running averages of $\overline{u'^2}$, $\overline{v'^2}$ for the smooth and tripped jets at random sample points.

has smeared the features observed in the instantaneous plots, but one still can see that the shear layer of the smooth jet extends to a higher r/D compared to the tripped case. Also, in the smooth case (figure 15b) regions with high vorticity expand to higher radial locations whereas in the tripped jet (figure 16b) there is a clear
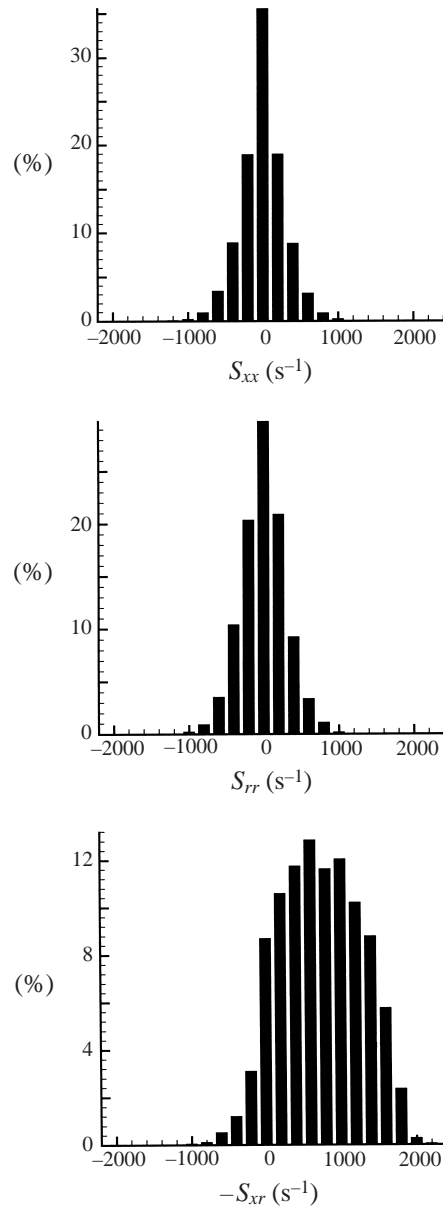
FIGURE 21. Distributions of strain rate elements in the region $0.45D < r < 0.58D$, $0.25D < x < 0.51D$ for the smooth jet.

peak at $x/D = 0.3$, $r/D \approx 0.5$. The regions of thinning vorticity and saddle points in velocity maps, in both the smooth and tripped cases, are consistent with the location of the trigger transducer during a positive pressure peak. It is evident that much of the difference between the smooth and tripped jets has been lost by phase averaging, indicating that our method of conditional sampling does not account for the variability caused by the 'secondary structures'. Consequently, there is still considerable turbulence in the phase-averaged data (figures 18 and 19).
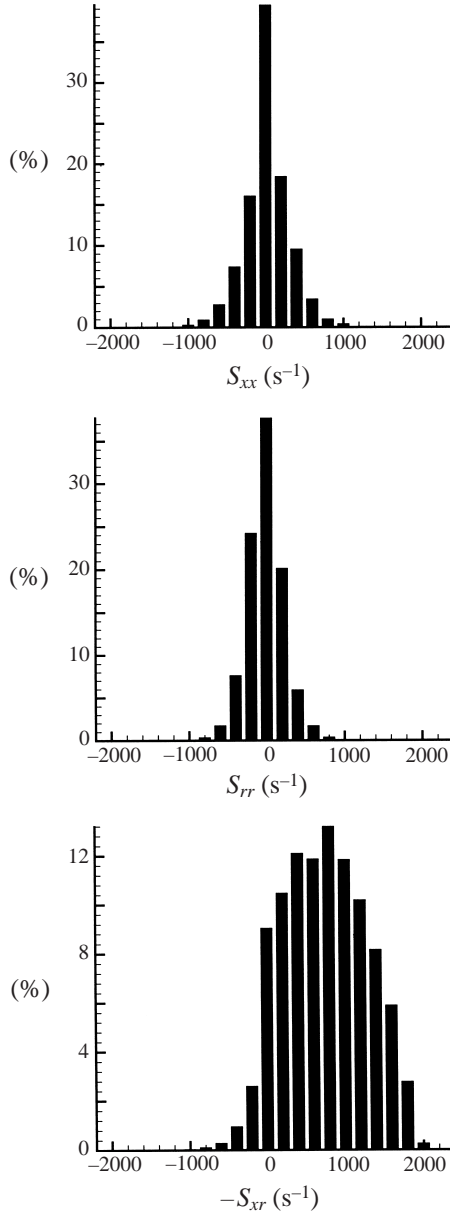
Figure 22. Distributions of strain rate elements in the region $0.43D < r < 0.56D$, $0.25D < x < 0.51D$ for the tripped jet.

5.3. *Reynolds stresses*

Distribution of turbulence stresses $\overline{u'^2}$, $\overline{v'^2}$ and $-\overline{u'v'}$ are plotted for the smooth and tripped cases in figures 18 and 19, respectively. Here $u' = u - \overline{u}$ and $v' = v - \overline{v}$ where (u, v) is the instantaneous velocity and $(\overline{u}, \overline{v})$ is the phase-averaged velocity. Sample running averages to determine whether the data are converged are plotted in figure 20. It is seen that convergence is not achieved, but since Reynolds stresses are not the primary focus of this paper, we did not pursue this issue. Several trends are evident from the results. First, magnitudes of $\overline{u'^2}$, $\overline{v'^2}$ and $-\overline{u'v'}$ are higher in the smooth

jet and they extend to higher radial locations than the corresponding values for the tripped jet. Second, there is a low level of fluctuations at the position corresponding to the trigger transducer. Third, there is no clear relationship between the location and magnitudes of the phase-averaged strains and shear stresses. In some cases, both are high at the same location (tripped jet at $x/D = 0.3$) but in others there are conflicting trends (smooth jet at $x/D = 0.25$). Fourth, in the smooth jet the peaks of the stresses consistently are located at $r/D > 0.5$, whereas in the tripped jet they are aligned with $r/D = 0.5$. In the tripped jet, the peaks coincide with peaks in the phase-averaged vorticity, but there is no obvious relationship in the smooth jet. Still, turbulent peaks in the smooth jet exist within regions of high vorticity; this suggest that the primary source of turbulence involves fluctuations in the locations (and strength) of the vortex structures. As noted in the introduction, the trends in the Reynolds stresses (especially maximum values in the untripped and tripped cases) are similar to measurements in a plane shear layer by Browand & Latigo (1979) and Bell & Mehta (1990). Our measurements of $\overline{u'^2}$ are remarkably similar to those by Browand & Latigo in a plane shear layer. Again $\overline{u'^2}$ is higher in the shear layer originating from a laminar boundary layer than the turbulent case for $x/\Theta < 800$ and asymptotes to almost same values downstream. Browand & Latigo's data show maximum normalized r.m.s. magnitudes for the laminar case to be 0.2 (at $x/\Theta \sim 200$), compared to 0.187 (at $x/\Theta \sim 100$ and 300) in our case. In the tripped case, their maximum value at $50 < x/\Theta < 200$ is about 0.14, which is the same in our case. This trend of the normal stresses in the very near field being higher in the untripped than in the tripped case is also observed in Bell & Mehta's (1990) measurements for a plane shear layer. Downstream the stresses asymptote to almost the same value, which cannot be seen in our case since our data extend up to $x/D = 0.72$. Highest (normalized) magnitudes of $\overline{u'^2}$ in Bell & Mehta's results are 0.06 for the untripped case, compared to 0.035 in our case and about 0.03 (at $x/\Theta \sim 175$) for the tripped case, compared to 0.02 in our case. Normalized magnitudes of $\overline{v'^2}$ are much higher in their results, reaching values of 0.11 in the untripped case compared to 0.018 in our case. Nevertheless, the value of $\overline{v'^2}$ in the untripped case is about 4 to 6 times the value for the tripped case, which is comparable to the factor of 3 in our case. Normalized magnitudes of $-\overline{u'v'}$ are comparable in the untripped and tripped cases (for $x/\Theta < 320$ or 175) and range from 0.007 to 0.014, similar to maximum values of 0.01 in our case.

5.4. *Distributions of strain tensor elements in smooth and tripped jets*

Figure 21 show distributions of $S_{xx}, S_{rr}, -S_{xr}$ in the smooth jet over the domain $0.25D \leqslant x \leqslant 0.5D$, $0.45D < r < 0.58D$, and a positive pressure peak at $x/D = 0.375$. The total number of points in this distribution is 8424. The domain selected is one wavelength in the axial direction. The mean shear strain in this domain satisfies $-\overline{S}_{xr}D/V_j \geqslant 1$. The corresponding domain selected for the tripped jet is $0.25D \leqslant x \leqslant 0.5D$, $0.43D < r < 0.56D$ and the total number of points is 8100. The distributions are presented in figure 22. Table 1 summarizes some of the properties of the strain distributions. The skewness and kurtosis are defined as

$$\text{skewness} = \frac{\sum(S - \overline{S})^3}{Nd^3}, \tag{5}$$

$$\text{kurtosis} = \frac{\sum(S - \overline{S})^4}{Nd^4}, \tag{6}$$

	Smooth jet			Tripped jet		
	S_{xx}	S_{rr}	$-S_{xr}$	S_{xx}	S_{rr}	$-S_{xr}$
Median (s^{-1})	0	0	600	0	0	800
Mean (s^{-1})	−3	−4	729	20	−15	741
Standard deviation (s^{-1})	285	295	541	286	233	532
Skewness	−0.05	0.04	−0.02	−0.03	0.08	0.03
Kurtosis	3.93	3.42	2.32	4.37	4.06	2.28

TABLE 1. Properties of strain distributions shown in figures 21 and 22.

where S is a strain component, $\overline{S}$ its mean, d its standard deviation and N is the total number of points. Table 1 shows that the mean shear strain of the tripped jet is slightly higher than that of the smooth jet. Also, it can be seen that mean shear strains are significantly higher than mean normal strains and that standard deviations of the shear strains are twice those of the normal strains. Thus, while in a very few individual realizations the magnitudes of shear and normal strains may be comparable, in most cases the shear strain dominates. Finally, there are no significant differences between the distributions of strain in the smooth and tripped jets.

5.5. *Estimation of principal strain rate*

For the purpose of determining the probability of peak negative pressures significant to cavitation inception, we also obtain strain distributions in the domain $0.25D \leqslant x \leqslant 0.5D$, $0.5D < r < 0.56D$ for the smooth jet. Recall that this wavelength (and phase) is the characteristic location of cavitation inception in the smooth jet. The distributions are shown in figure 23 and some of the parameters are summarized in table 2. The total number of points in this distribution is 4590. Again the mean value of $-S_{xr}$ is significantly higher than mean values of S_{xx} and S_{rr}, and its standard deviation also is higher. We will now estimate the direction and magnitude of the principal strain rate, so that the stretching of streamwise vortices can be calculated. These vortices are stretched by a strain rate $S_{\eta\eta}$ where ζ, η are the axes after rotating the original axes x, r by α degrees counter clockwise and

$$S_{ij} = \frac{1}{2}\left(\frac{\partial u_i}{\partial x_j} + \frac{\partial u_j}{\partial x_i}\right).$$

Using the general transformation formula (Batchelor 1967),

$$S'_{ij} = \frac{\partial r_k}{\partial r'_i}\frac{\partial r_l}{\partial r'_j}S_{kl}, \tag{7}$$

where prime denotes the transformed system,

$$S_{\eta\eta} = -S_{xr}\sin 2\alpha + 2S_{xx}\sin^2\alpha + 2S_{rr}\cos^2\alpha. \tag{8}$$

The direction of the average principal strain rate is then

$$\tan 2\alpha = \frac{-\overline{S}_{xr}}{\overline{S}_{rr} - \overline{S}_{xx}}. \tag{9}$$

Using the mean values listed in table 2, we get $2\alpha = 93.13°$ or $\alpha \approx 45°$. This shows that the principal strain axis typically is aligned at about 135° to the direction of flow,
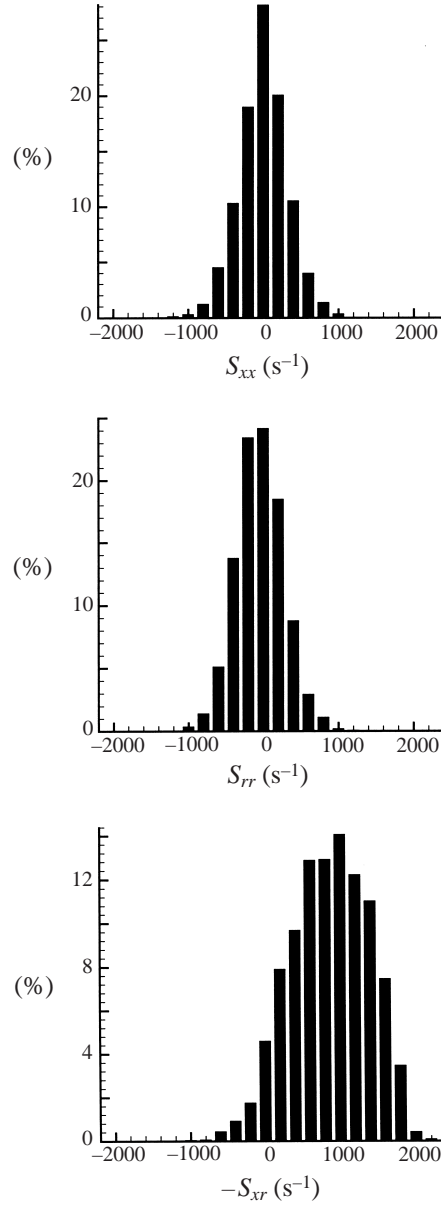
FIGURE 23. Distributions of strain rate elements for the smooth jet in the region $0.5D < r < 0.56D$, $0.25D < x < 0.51D$: the region of cavitation inception.

which matches well with the inclination of the cylindrical bubbles in figures 7(a) and 7(b). From (8), with $\alpha \approx 45°$, the principal strain rate is

$$S_{\eta\eta} = -S_{xr} + S_{xx} + S_{rr}. \tag{10}$$

The distribution of $S_{\eta\eta}$ is shown in figure 24 and its properties in table 2. The mean of $S_{\eta\eta}$ is comparable to $-\bar{S}_{xr}$, but its standard deviation is higher. In §8, $S_{\eta\eta}$ is used for estimating the probability of pressure coefficients less than $-\sigma$.
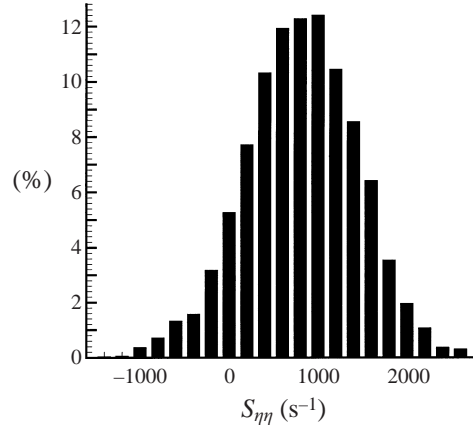
FIGURE 24. Strain rate distribution at 135° to the direction of flow (i.e. principal strain rate) in the region $0.25D \leqslant x \leqslant 0.5D$, $0.5D \leqslant r \leqslant 0.56D$ for the smooth jet.

	S_{xx}	S_{rr}	$-S_{xr}$	$S_{\eta\eta}$
Median (s^{-1})	0	0	1000	800
Mean (s^{-1})	−1	−48	860	811
Standard deviation	321	316	523	629
Skewness	−0.056	0.135	−0.256	−0.157
Kurtosis	3.47	3.23	2.57	3.12

TABLE 2. Properties of the strain distributions for a smooth jet in the region $0.25D \leqslant x \leqslant 0.5D$, $0.5D < r < 0.56D$ (figures 23 and 24).

6. Measurement of velocity field in planes that cut through the streamwise vortices

Data were recorded at planes parallel to the jet axis at $r \cos \Phi = 0.53D$ and $0.55D$ (figure 5). The details of the experimental procedure are explained in § 2.1.4. Although the exact orientation of the streamwise vortices is not known, the vorticity obtained in this interrogation plane can give reasonable estimates of the strengths of these vortices, if the plane cuts through an entire vortex.

Figures 25, 26, 27 and 28 show sample instantaneous velocity and vorticity field for the smooth and the tripped cases. All the vorticity maps show vortical regions that appear elongated, since the interrogation plane cuts through these structures at varying angles, depending on their location and orientation. The distributions also show counter-rotating vortices spaced about $0.05D$ apart, which is one signature of a hairpin vortex (the other being the radially displaced vortex in the vorticity distributions in figures 11b, 11d–f). Also note that the vorticity map for the smooth jet (figure 25b) shows a larger number of vortical regions compared to figure 26(b) for the tripped jet. At the plane $r \cos \Phi = 0.55D$ in both cases there is very little vortical fluid up to $0.4D$, which is consistent with the radial spread of vorticity in figures 11(b), 11(d–f).

Forty-two images were analysed at the plane $r \cos \Phi = 0.53D$ in both cases, to obtain a distribution of the strength of the streamwise vortices. Since we were primarily interested in the estimation of peak negative pressures (relevant to cavitation
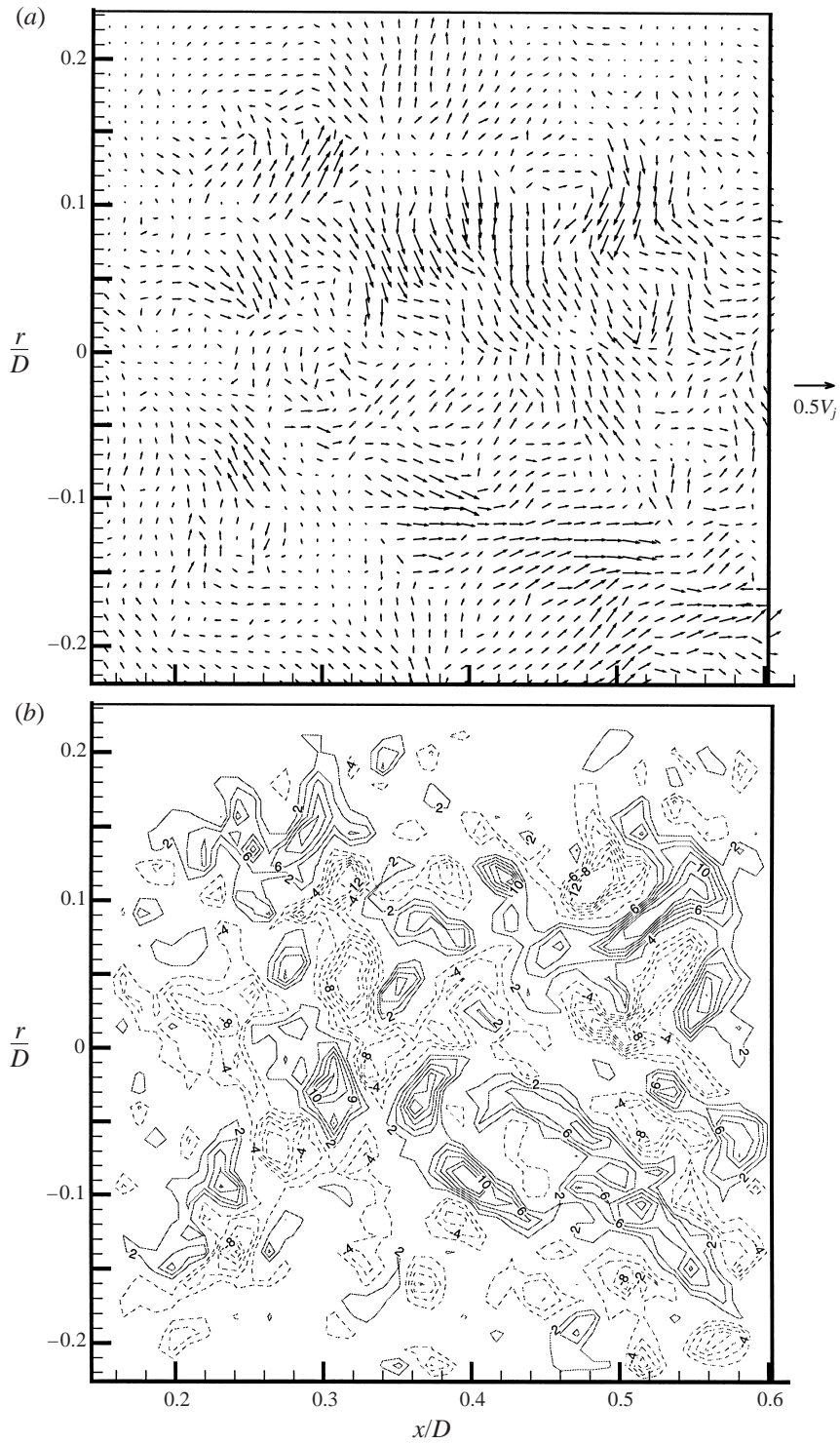
FIGURE 25. Sample instantaneous (*a*) velocity, (*b*) normalized vorticity ($\omega D/V_j$) in the plane $r \cos \Phi = 0.53D$ for the smooth jet. Increment in contour lines is 2. Zero is not shown. Dashed lines represent negative vorticity.

FIGURE 26. As figure 25 but for the tripped jet.

FIGURE 27. Sample instantaneous (*a*) velocity, (*b*) normalized vorticity ($\omega D/V_j$), in the plane $r\cos\Phi = 0.55D$ for the smooth jet. Increment in contour lines is 2. Zero is not shown. Dashed lines represent negative vorticity.
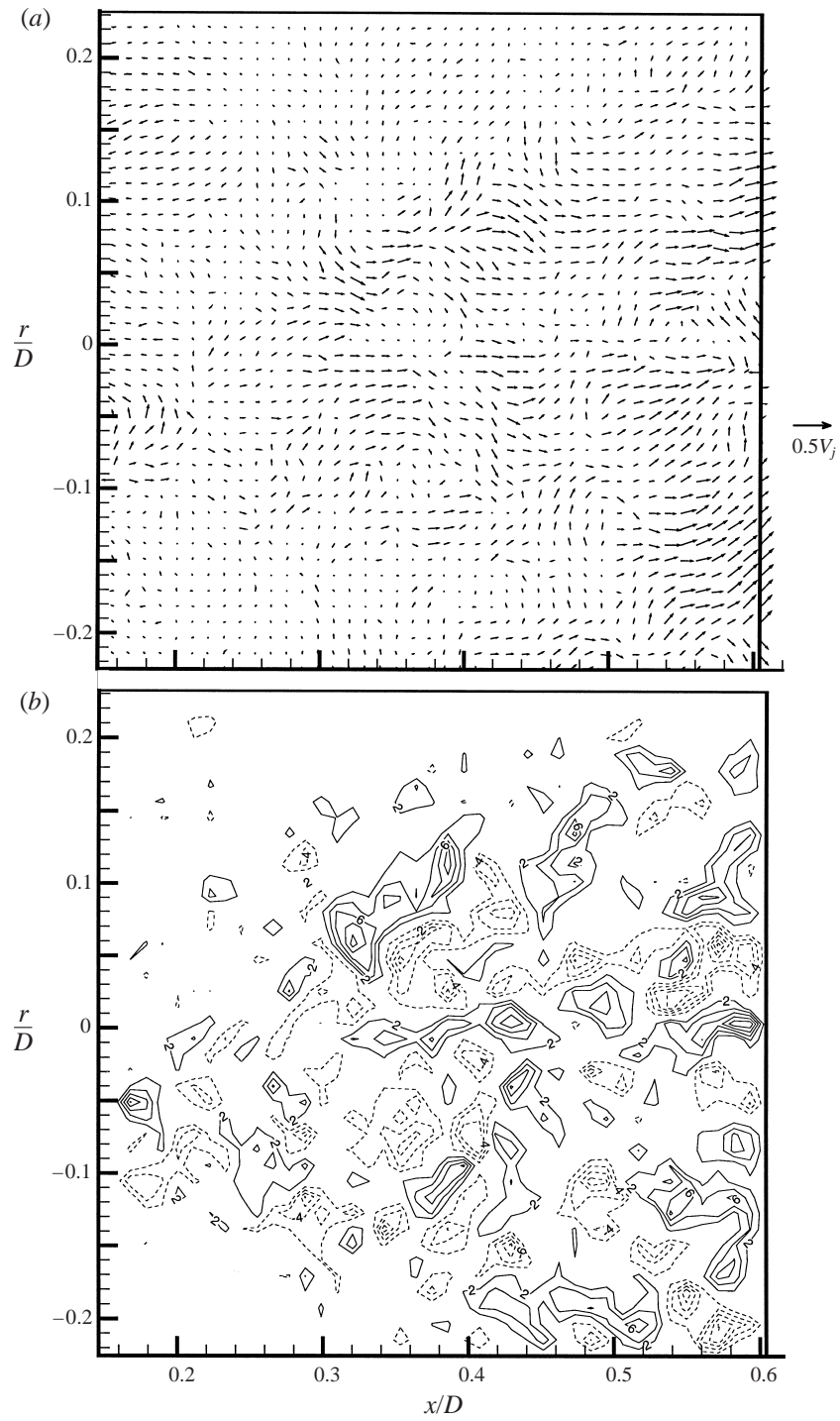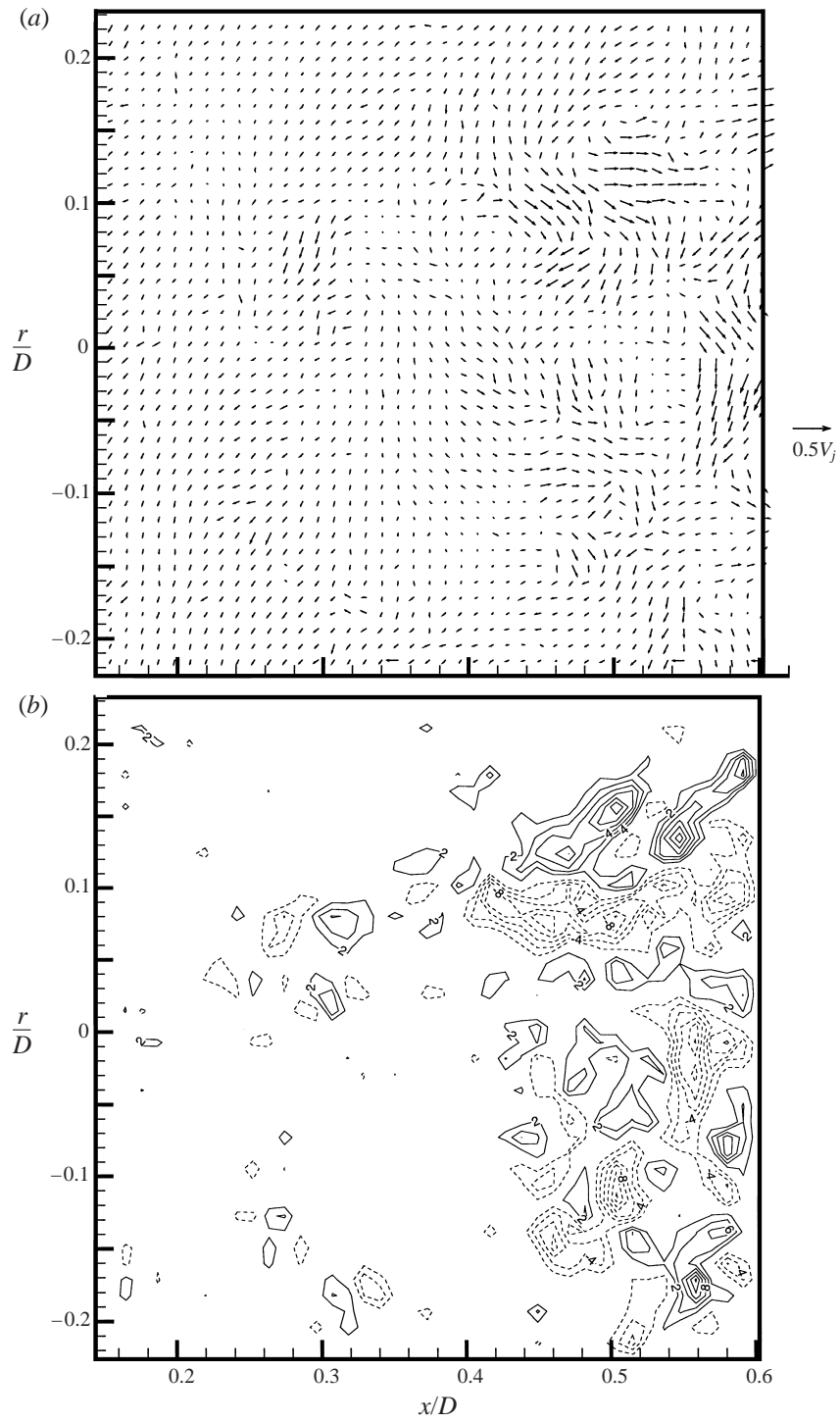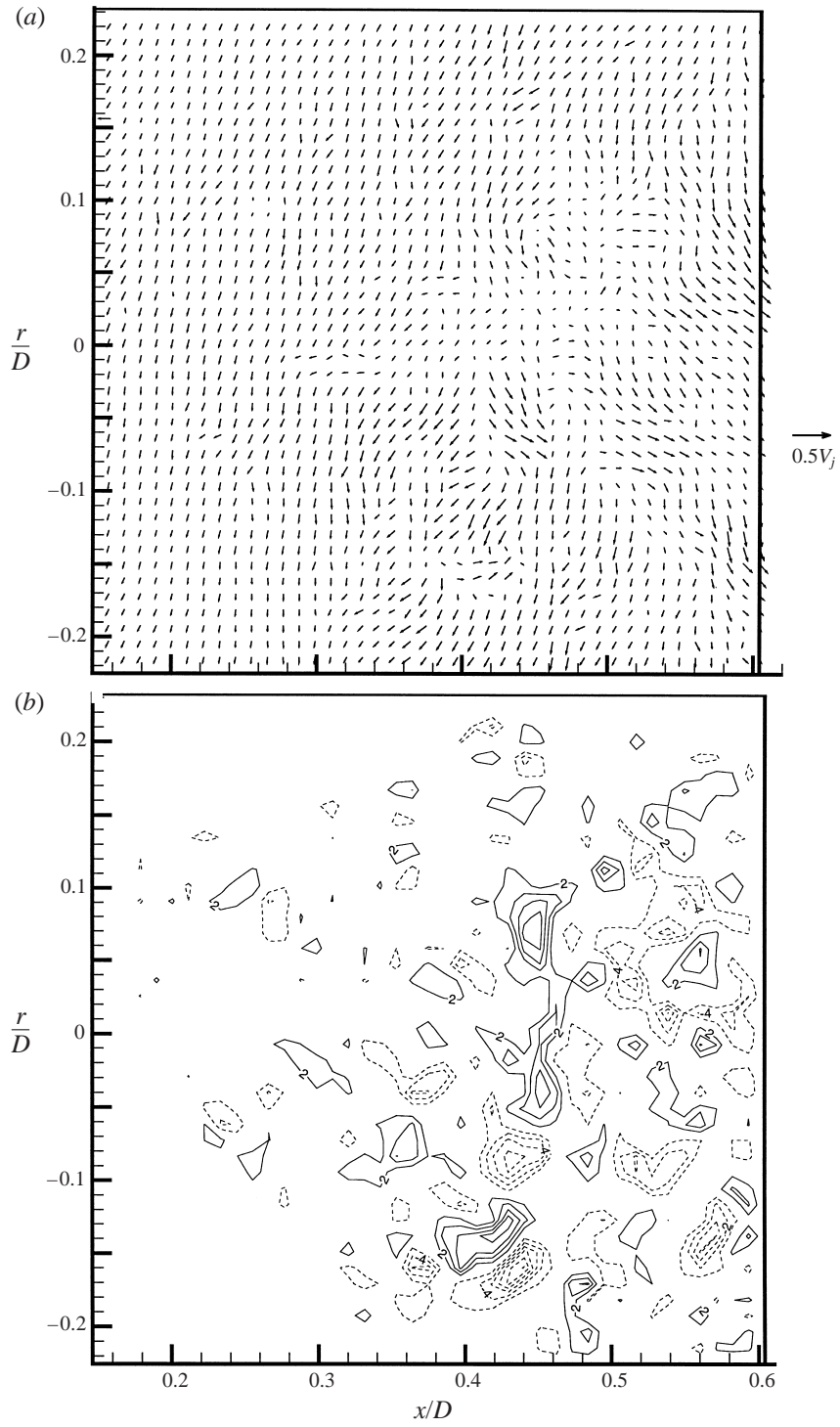
(a)

(b)

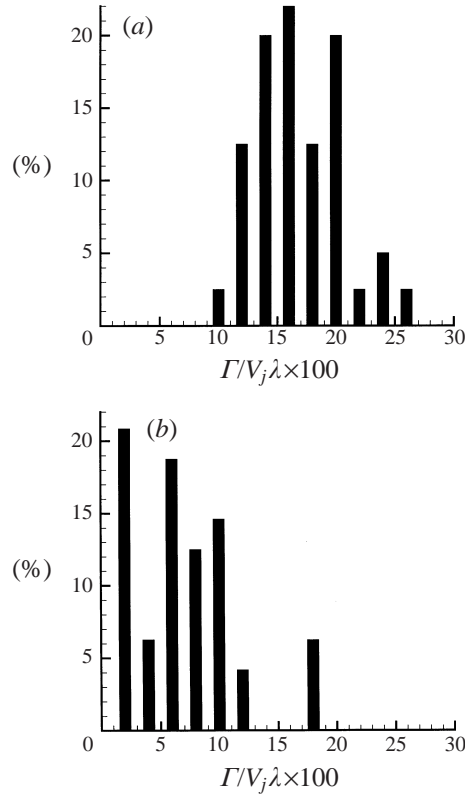FIGURE 28. As figure 27 but for the tripped jet.

FIGURE 29. Distribution of highest strengths (in 42 instantaneous maps) of streamwise vortices for (a) smooth, (b) tripped, jet in the plane $r \cos \Phi = 0.53D$ and $0.15D < x < 0.6D$.

inception), the highest circulation value was chosen from every instantaneous map for both the smooth and tripped jets. The strengths were calculated using,

$$\Gamma = \sum_R \omega_i \, \mathrm{d}A_i \tag{11}$$

where $\mathrm{d}A$ is the elemental area $= 539 \times 539 \, \mu\mathrm{m}^2$. R is a closed region of vorticity of the same sign, with a vorticity distribution that has peak magnitudes at the centre and tapers to a lower value at the boundary. A typical region R spans 4–5 data points along the minor axis and 7–10 data points along the major axis. Note that these distributions are bigger than the actual vortex for two reasons: (i) the velocity data are obtained over a region $900 \times 900 \, \mu\mathrm{m}^2$ with an overlap of about 40%. This clearly smears the velocity field of the vortex, (ii) the vorticity is calculated from the velocity field using centred differences. This adds to the smearing effect, giving a distribution larger than the actual one. Considering these effects, it can be estimated from these distributions that the size (effective diameter) of the structure would vary from 800 μm to 2 mm. It would have been better to integrate the velocity field on a simple path around the vortex to estimate their strengths. But vortices lying close to each other made it very difficult to choose a suitable circuit around a structure. The strength distributions are shown in figure 29 for the smooth and the tripped jets. The abscissa for these plots is $\Gamma / V_j \lambda$, where, $\lambda = 0.25D$ and $V_j \lambda$ is the total circulation within a wavelength. The distributions show that peaks for the smooth

and the tripped nozzle occur at 16% and 2% of $V_j\lambda$ respectively. Strengths above 19% of $V_j\lambda$ occur 30% of the time for the smooth jet, and 0% for the tripped jet. Thus, the secondary vortices in the smooth jet are very much stronger than those in the tripped jet. This striking result identifies the primary difference between the two cases. Studies by O'Hern (1990) in a plane shear layer estimated (using core pressure measurements) that $\Gamma_s/\Gamma_p \leqslant 0.1$, where Γ_s is the strength of the secondary vortex and Γ_p is the strength of a spanwise (primary) vortex (i.e. $V\lambda$). Although, the streamwise vortices in his studies had strengths in the range 0.02–0.12 $\mathrm{m^2\,s^{-1}}$ (as compared to a maximum of 0.033 $\mathrm{m^2\,s^{-1}}$ in the present smooth jet), the relative strengths Γ_s/Γ_p in his case were much lower than in the present smooth jet. Bell & Mehta (1993) performed experiments with a plane shear layer at $Re_\delta = 2.9 \times 10^4$, with untripped and tripped boundary layers. They found the average streamwise circulation to be 10% of the spanwise circulation, for the untripped case (at axial locations higher than ours). On tripping the boundary layer, they did not observe spatially stationary streamwise vortices. The tripped jet in the present study shows a relative strength $\Gamma/V_j\lambda \leqslant 0.12$ (about 93% of the time), whereas the smooth jet shows $\Gamma/V_j\lambda \leqslant 0.27$. This trend of diminishing three-dimensionality on tripping the boundary layer is consistent with Bell & Mehta's data.

In summary, the results show that a secondary vortex in the very near field of the smooth jet can have up to a quarter of the circulation per wavelength, highlighting the strong three-dimensionality of the near field. The impact of these results on peak negative pressures in the near field and cavitation inception is discussed in §8.

7. Measurements of the separating boundary layer

To complete the picture of the near-field flow, one needs the characteristics of the separating boundary layer. The global jet parameters, namely the diameter, the Reynolds number, the Strouhal number based on the diameter ($St_D \approx 1.0$ at $x/D = 0.375$) and wavelength $\lambda = 0.25D$ (both for the untripped case) have already been given. In this section we provide data on the initial momentum thickness, Θ, and the shape factor of the smooth and tripped boundary layers. Experimental details are provided in §2.1.3.

Figure 30(a) shows a phase-averaged velocity profile for the smooth jet, collected from 18 vector maps, at two locations $x/D = 0.0073$ and 0.042. Figure 30(b) shows the velocity profiles for the tripped boundary layer at two locations $x/D = 0.0071$ and 0.047. Table 3 gives the displacement thickness (δ^*), momentum thickness (Θ), the shape factor δ^*/Θ, $Re_\Theta = V_j\Theta/\nu$ and Θ/D calculated from the velocity profiles. The results are compared to classical data taken from Burmeister (1993) for a flat plate and to those of Hussain & Zedan (1978) for a circular jet. The drop in the shape factor of the boundary layer from 3.4 to 2.07 due to tripping is consistent with a turbulent boundary layer after it transitions from laminar. For a flat plate, shape factors ranging from 2.55 to 1.4 correspond to the region of transition. Thus, tripping the boundary layer has doubled the initial momentum thickness, and causes transition to turbulence. Hence, it is important to note that the differences that have been observed in the near-field flow structure are not merely an effect of the (initial) momentum thickness being doubled, but also the fact that it is turbulent. Velocity profiles at $x/D = 0.042$ and 0.047 show clear evidence of diffusion in both cases which, as expected, is higher in the tripped case.
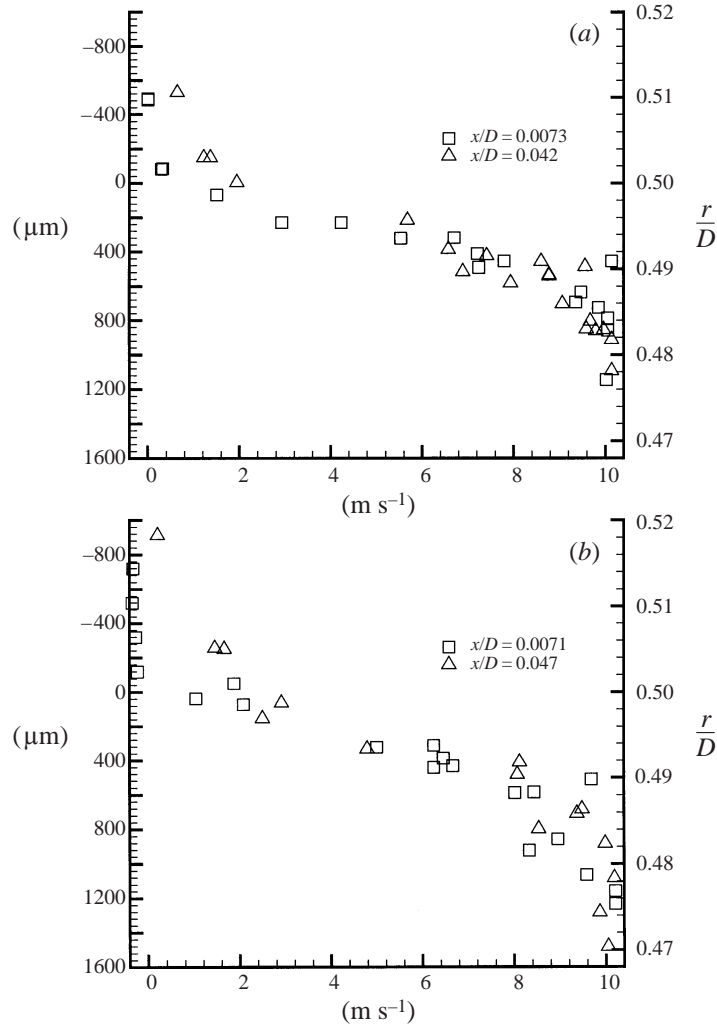
FIGURE 30. Velocity profiles of the separating boundary layer for (*a*) smooth jet, (*b*) tripped jet, at two axial locations.

8. Estimation of rate of cavitation events for the untripped jet

As seen in § 3, cavitation inception indices of the present untripped jet reach levels of 2.5 and appear as cylindrical bubbles in the near field. These indices are considerably higher than most of the data reported in earlier experiments (figure 1). Earlier experiments with a 25 mm jet at the same facility yielded a cavitation inception index of 1.0 at the same Reynolds number and 1.62 at $Re_D = 3 \times 10^5$ (Ran & Katz 1994). Are such high inception indices reasonable? This question can be answered by estimating the peak pressure coefficient in the cores of the streamwise vortices, in the region $0.25D \leqslant x \leqslant 0.5D$, $0.5D < r < 0.56D$ where cavitation inception occurred. The measured strain rates and strengths of streamwise vortices enable us to estimate the probability distribution of core pressures as a function of σ, the dimensionless ambient pressure. Using the spatial distribution of bubbles (nuclei) one can then

	δ^* (μm)	Θ (μm)	Shape factor δ^*/Θ	Re_Θ	Θ/D $\times 10^3$
Smooth jet	393	110	3.4	1100	2.2
Tripped jet	417	201	2.07	2010	4.02
Laminar boundary layer (flat plate, Burmeister 1993)	—	—	2.6	—	—
Turbulent boundary layer (flat plate, Burmeister 1993)	—	—	1.3	—	—
Laminar boundary layer in circular jet, from Hussain & Zedan (1978)	—	107–351	2.37–2.6	204–349	1.4–4.6
Turbulent boundary layer in circular jet, from Hussain & Zedan (1978)	—	262–483	1.51–1.6	215–890	3.4–6.3

TABLE 3. Boundary layer data at $x/D = 0.0073$ for the smooth jet and $x/D = 0.0071$ for the tripped jet.

calculate the rate of cavitation events and compare with the experimental values in figure 9.

From §5.5, the extensional strain in the streamwise vortex aligned approximately at $135°$ to the direction of flow is

$$\frac{\mathrm{d}l}{l} = S_{\eta\eta}\,\mathrm{d}t, \quad l = l_0\,\mathrm{e}^{S_{\eta\eta}\Delta t}, \tag{12}$$

where l_0 is the original length of the vortex and l is the length after a time interval Δt. If d_0 is the original diameter of the vortex then from mass conservation

$$d = d_0\sqrt{l_0/l},$$

where d is the diameter after Δt.

From equation (12),

$$d = d_0\,\mathrm{e}^{-S_{\eta\eta}\Delta t/2}. \tag{13}$$

Some estimates for Δt and d_0 are as follows:

$$\Delta t \sim \frac{\lambda}{V_j} = 1.25\,\mathrm{ms}, \tag{14}$$

$$d_0 \sim 1\,\mathrm{mm}. \tag{15}$$

The choice of this diameter is discussed in §6. In reality, the diameter could vary from $800\,\mu\mathrm{m}$ to $2\,\mathrm{mm}$. For a maximum strain rate of $S_{\eta\eta} = 2600\,\mathrm{s}^{-1}$, from equation (13), $d \approx 200\,\mu\mathrm{m}$. The diffusion length scale during this time interval $\sqrt{\nu\Delta t}$ is $35\,\mu\mathrm{m}$, which is 17.5% of the final diameter in the present case. Hence, viscous diffusion during this time period is very much confined within the core of the vortex. On the other hand if the initial diameter is about $200\,\mu\mathrm{m}$, the diffusion length scale and the final diameter have the same magnitude. In such a case the axial straining will be balanced by viscous diffusion and the vortex reaches a minimum size.

With a Rankine vortex model, we now estimate the probability that the peak pressure coefficient in the core of the stretched vortex is lower than $-\sigma$.

For the flow induced by Rankine vortex

$$\frac{\partial P}{\partial r} = \frac{\rho v_t^2}{r},$$ (16)

where v_t is the tangential velocity at a radial distance r from the centre of the vortex and Γ is the strength. Outside of the core, $v_t = \Gamma/2\pi r$ and inside the core, $v_t = 0.5\omega r$.

Integrating equation (16) from $r = 0$ to $r \to \infty$ gives

$$P_\infty - P_c = \frac{\rho \Gamma^2}{\pi^2 d^2}.$$

Thus the pressure coefficient in the core of the vortex is

$$C_{pc} = \frac{P_c - P_\infty}{0.5\rho V_j^2} = -\frac{2}{\pi^2}\left(\frac{\Gamma}{V_j d}\right)^2 = -\frac{2}{\pi^2}\left(\frac{\Gamma}{V_j \lambda}\right)^2 \left(\frac{\lambda}{d}\right)^2.$$ (17)

Consequently (from (13)) the critical strain rate S_{cr} for $C_{pc} = -\sigma$ is

$$S_{cr}(\Gamma, \sigma) = \frac{1}{\Delta t} \ln\left(\frac{0.5\pi^2 \sigma d_0^2}{(\Gamma/V_j\lambda)^2 \lambda^2}\right).$$ (18)

Assuming that the strength of the vortex and the strain field it is subjected to are independent events, the probability of $C_{pc} \leqslant -\sigma$ is

$$\Pi(C_{pc} \leqslant -\sigma) = \sum_i \Pi(\Gamma = \Gamma_i)\Pi(S_{\eta\eta} \geqslant S_{cr}^i),$$ (19)

where Π denotes probability, Γ_i are the highest strengths of the vortices shown in figure 29(*a*) and S_{cr}^i is S_{cr} for $\Gamma = \Gamma_i$ in equation (18).

To estimate the rate of cavitation events (r_c), we need to combine (19) with the availability of nuclei. The average number of bubbles (nuclei) available to one vortex ($\bar{n}_v$) can be estimated as follows. From the bubble injection rate of approximately 16 000 bubbles per second, number of bubbles per wavelength, n_λ, is 78. Part of this is entrained by the spanwise vortex, leading to a non-uniform bubble distribution. Based on the data in figure 10(*a*), the average concentration of bubbles in the cavitation inception region is only 80% of the average concentration. Thus,

$$\bar{n}_v = 0.8\beta_v n_\lambda,$$ (20)

where β_v is the volume fraction of the stretched vortex. A stretched vortex has a diameter of the order of 500 μm (from equation (13)) and a length of $b\cos 45°$, where b is the shear layer thickness. Then,

$$\beta_v = \frac{(\pi/4)d^2 b}{(0.46D)(0.18D)b\cos 45°}, \quad \bar{n}_v = 0.08.$$ (21)

The measurements in §6 show that there are about 1.5 vortices in a volume that corresponds to the region of cavitation. Since the weaker vortex (with a weight of 0.5) will have little contribution in the onset of cavitation we consider only the highest one, whose distribution is known. Then,

$$r_c = St_D \frac{V_j}{D} \bar{n}_v \Pi\,(C_{pc} \leqslant -\sigma),$$ (22)

where $St_D \approx 1$.

The results are shown in figure 31 and compared with the measured data. One set
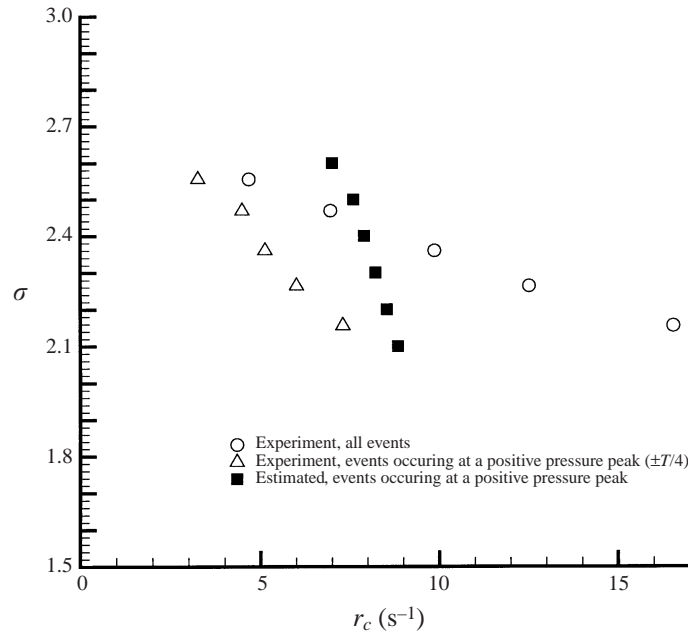
FIGURE 31. Estimated rate of cavitation events compared with measured number of
events for the smooth jet.

of points shows all the measured events, which was introduced in figure 9, and the
other set corresponds to the measured events that occurred when the pressure near
the trigger transducer is high ($\pm T/4$), i.e. similar to the experimental conditions used
for predicting the events. It is evident that at high σ, there is relatively little difference
between the total number of measured events and those occurring during a positive
pressure peak (4.5 vs. 3 at $\sigma = 2.56$), i.e. the majority of the events occur during the
phase that has been investigated in this paper. As σ is reduced the differences increase,
presumably since the pressure becomes low enough to cause cavitation during other
phases. We prefer not to speculate on these trends beyond this qualitative statement,
since it would require a comparison to flow structures that are not investigated at
the same level of detail, as well as nuclei distributions after inception has already
occurred. At high σ, the estimated rate of cavitation events is about twice (~ 7 at
$\sigma = 2.56$) the measured value at the same phase. Considering the simplified means
used to estimate the event rate (based on measured nuclei distributions as well as
the strength and straining of secondary vortices), the agreement with the measured
results at high σ is remarkable. These results confirm that the type of structures that
exist in the shear layer, and the type of straining to which they are exposed, can
lead to the observed cavitation phenomena. However, the estimated rate increases less
rapidly than the measured values with decreasing σ. This difference in the trends is
probably caused by two effects. First, as σ is reduced, as mentioned earlier, cavitation
occurs also in other phases, which would cause the same change in slope as in the
measured data (increase the event rate). Second, when cavitation inception occurs, it
dramatically increases the concentration and distribution of nuclei available for the
vortices. Consequently, the number of events should be higher than those occurring
with the pre-cavitation nuclei distribution. Quantifying this 'nonlinear' effect requires
at least measurements of the production of nuclei and their spatial distribution during

early stages of cavitation. As σ decreases further, one has to account also for the effect of the cavitation on the flow structure. Such measurements are beyond the scope of the present study.

9. Conclusions

A 50 mm jet ($Re_D = 5 \times 10^5$) with an initially laminar boundary layer at $Re_\Theta = 1100$ ($\delta^*/\Theta = 3.4$), showed transition to three-dimensional flow in the near field with strong streamwise vortical structures. Cavitation inception occurred within the core of these vortices. The strengths of these vortices reached levels of 25% of $V_j\lambda$ with inception indices of 2.5. Tripping the boundary layer increased Re_Θ to 2010 and reduced δ^*/Θ to values characteristic of a turbulent velocity profile. It also resulted in formation of the familiar Kelvin–Helmholtz vortex rings with significantly weaker secondary vortices. Cavitation inception now occurred further downstream ($x/D \approx 2$) in the cores of the primary vortices with inception indices of 1.7. In addition to the effect on the inception index the results demonstrate the substantial impact that small changes to the boundary layer have on the transition region in the near field of jets. This sensitivity to initial conditions should be accounted for while attempting to simulate such flows, especially using LES where resolution in an issue. Using the measured strengths and stretching of the streamwise vortices as well as the bubble (nuclei) distributions the rate of cavitation events was estimated as a function of the cavitation index. The predicted results agree very well with the measured cavitation rates.

REFERENCES

ADRIAN, R. J. 1991 Particle-imaging techniques for experimental fluid mechanics. *Ann. Rev. Fluid Mech.* **23**, 261.

ARNDT, R. E. A. 1981 Cavitation in fluid machinery and hydraulic structures. *Ann. Rev. Fluid Mech.* **13**, 273–328.

ARNDT, R. E. A. 1995 Vortex cavitation. In *Fluid Vortices* (ed. S. I. Green), pp. 731–782. Springer.

BATCHELOR, G. K. 1967 *An Introduction to Fluid Dynamics.* Cambridge University Press.

BELAHADJI, B., FRANC, J. P. & MICHEL, J. M. 1995 Cavitation in the rotational structures of a turbulent wake. *J. Fluid Mech.* **287**, 383–403.

BELL, J. H. & MEHTA, R. D. 1990 Development of a two-stream mixing layer from tripped and untripped boundary layers. *AIAA J.* **28**, 2034–2042.

BELL, J. H. & MEHTA, R. D. 1993 Effects of imposed spanwise perturbations on plane mixing-layer structure. *J. Fluid Mech.* **257**, 33–63.

BERNAL, L. P. 1981 The coherent structure in turbulent mixing layers. II. Secondary streamwise vortex structure. PhD thesis, Caltech.

BERNAL, L. P. & ROSHKO, A. 1986 Streamwise vortex structure in plane mixing layers. *J. Fluid Mech.* **170**, 499–525.

BERTUCCIOLI, L., GOPALAN, S. & KATZ, J. 1996 Image shifting for PIV using birefringent and ferroelectric liquid crystals. *Exps. Fluids* **21**, 341–346.

BREIDENTHAL, R. E. 1981 Structure in turbulent mixing layers and wakes using a chemical reaction. *J. Fluid Mech.* **116**, 1–24.

BRENNEN, C. E. 1995 *Cavitation and Bubble Dynamics.* Oxford University Press.

BROWAND, F. K. & LATIGO, B. O. 1979 Growth of the two-dimensional mixing layer from a turbulent and nonturbulent boundary layer. *Phys. Fluids* **22**, 1011–1019.

BURMEISTER, L. C. 1993 *Convective Heat Transfer.* John Wiley & Sons.

DONG, R., CHU, S. & KATZ, J. 1992 Quantitative visualization of the flow structure within the volute of a centrifugal pump, Part A: Technique, *Trans. ASME* I: *J. Fluids Engng* **114**, 390–395.

HUSSAIN, A. K. M. F. 1986 Coherent structure and turbulence. *J. Fluid Mech.* **173**, 303–356.

HUSSAIN, A. K. M. F. & ZEDAN, M. F. 1978 Effects of the initial condition on the axisymmetric free shear layer: effects of the initial momentum thickness. *Phys. Fluids* **21**, 1100–1112.

JIMENEZ, J. 1983 A spanwise structure in the plane mixing layer. *J. Fluid Mech.* **132**, 319–336.

JIMENEZ, J., COGOLLOS, M. & BERNAL, L. P. 1985 A perspective view of the plane mixing layer. *J. Fluid Mech.* **152**, 125–143.

JOHNSON, V. E., CHAHINE, G. L., LINDENMUTH, W. T., CONN, A. F., FREDERICK, G. S. & GIACCHINO, G. J. 1982 Cavitating and structured jets for mechanical bits to increase drilling rate. *ASME Paper* 82-Pet-13, Energy Sources Technology Conference and Exhibition, March 7–10, New Orleans, LA.

JOSEPH, D. D. 1998 Cavitation and the state of stress in a flowing liquid. *J. Fluid Mech.* **366**, 367–378.

KATZ, J. 1984 Cavitation phenomena within regions of flow separation. *J. Fluid Mech.* **140**, 497–536.

KATZ, J. & O'HERN, T. J. 1986 Cavitation in large scale shear flows. *Trans ASME* I: *J. Fluids Engng* **108**, 373–376.

KERMEEN, R. W. & PARKIN, B. R. 1957 Incipient cavitation and wake flow behind sharp-edged disks. *Cal. Inst. Tech., Hydrodyn. Lab. Rep.* 85-4.

KOBAYASHI, R. 1967 Effect of cavitation on the discharge coefficient of standard flow nozzles. *Trans. ASME* D: *J. Basic Engng* **89** (3), 677–685.

KONRAD, J. H. 1976 An experimental investigation of mixing in two-dimensional turbulent shear flows with applications to diffusion-limited chemical reactions. PhD thesis, Caltech.

KUHN DE CHIZELLE, Y., CECCIO, S. L. & BRENNEN, C. E. 1995 Observations and scaling of travelling bubble cavitation. *J. Fluid Mech.* **293**, 99–126.

LASHERAS, J. C., CHO, J. S. & MAXWORTHY, T. 1986 On the origin and evolution of streamwise vortical structures in a plane, free shear layer. *J. Fluid Mech.* **172**, 231–258.

LASHERAS, J. C. & CHOI, H. 1988 Three-dimensional instability of a plane free shear layer: an experimental study of the formation and evolution of streamwise vortices. *J. Fluid Mech.* **189**, 53–86.

LIU, Z. & BRENNEN, C. E. 1998 Cavitation nuclei population and event rates. *Trans. ASME* I: *J. Fluids Engng* **120**, 728–737.

O'HERN, T. J. 1990 An experimental investigation of turbulent shear flow cavitation. *J. Fluid Mech.* **215**, 365–391.

OOI, K. K. & ACOSTA, A. J. 1983 The utilization of specially tailored air bubbles as static pressure sensors in a jet. *Trans. ASME* I: *J. Fluids Engng* **106**, 459–465.

PAUCHET, J., RETAILLEAU, A. & WOILLEZ, J. 1992 The prediction of cavitation inception in turbulent water jets. *ASME Cavitation and Multiphase Flow Forum* **135**, 149–158.

PLESSET, M. S. & PROSPERETTI, A. P. 1977 Bubble dynamics and cavitation. *Ann. Rev. Fluid Mech.* **9**, 145–185.

RAN, B. & KATZ, J. 1991 The response of microscopic bubbles to sudden changes in ambient pressure. *J. Fluid Mech.* **224**, 91–115.

RAN, B. & KATZ, J. 1994 Pressure fluctuations and their effect on cavitation inception within water jets. *J. Fluid Mech.* **262**, 223–263.

ROTH, G., HART, D. & KATZ, J. 1995 Feasibility of using the L64720 video motion estimation processor (MEP) to increase efficiency of velocity map generation for PIV. *ASME/EALA Sixth Intl Symp. On Laser Anemometry, Hilton Head, SC.*

SINHA, M. & KATZ, J. 1998 Flow structure & turbulence in a centrifugal pump with a vaned diffuser. *Proc. ASME Fluids Engng Div. Washington DC.*

SRIDHAR, G. & KATZ, J. 1995 Lift and drag forces on microscopic bubbles entrained by a vortex. *Phys. Fluids* **7**, 389–399.

STRASBERG, M. 1956 Gas bubbles as sources of sounds in liquids. *J. Acoust. Soc. Am.* **28**, 21–26.